

JGR Solid Earth

RESEARCH ARTICLE

10.1029/2021JB023173

Key Points:

- Contributions of grain size reduction and CPO development to strain weakening in ice are quantified using experimental data
- Strain weakening can be accounted for entirely using constitutive flow laws that account for CPO development; grain size plays a negligible role
- Glaciological and geodynamic models need to account for CPO development in viscously anisotropic minerals like ice, olivine, and quartz

Supporting Information:

Supporting Information may be found in the online version of this article.

Correspondence to:

S. Fan,
sheng.fan@otago.ac.nz

Citation:

Fan, S., Cross, A. J., Prior, D. J., Goldsby, D. L., Hager, T. F., Negrini, M., & Qi, C. (2021). Crystallographic preferred orientation (CPO) development governs strain weakening in ice: Insights from high-temperature deformation experiments. *Journal of Geophysical Research: Solid Earth*, 126, e2021JB023173. <https://doi.org/10.1029/2021JB023173>

Received 4 SEP 2021
Accepted 1 DEC 2021

Author Contributions:

Conceptualization: Sheng Fan, David J. Prior

Data curation: Sheng Fan, Travis F. Hager, Marianne Negrini, Chao Qi



Formal analysis: Sheng Fan

Funding acquisition: Sheng Fan, David J. Prior, David L. Goldsby

Methodology: Sheng Fan, Andrew J. Cross, David J. Prior, David L. Goldsby, Travis F. Hager

Software: Sheng Fan, Andrew J. Cross

Crystallographic Preferred Orientation (CPO) Development Governs Strain Weakening in Ice: Insights From High-Temperature Deformation Experiments

Sheng Fan¹ , Andrew J. Cross² , David J. Prior¹ , David L. Goldsby³ , Travis F. Hager³, Marianne Negrini¹, and Chao Qi⁴ 

¹Department of Geology, University of Otago, Dunedin, New Zealand, ²Department of Geology and Geophysics, Woods Hole Oceanographic Institution, Woods Hole, MA, USA, ³Department of Earth and Environmental Science, University of Pennsylvania, Philadelphia, PA, USA, ⁴Institute of Geology and Geophysics, Chinese Academy of Sciences, Beijing, China

Abstract Strain weakening leads to the formation of high-strain shear zones and strongly influences terrestrial ice discharge. In glacial flow models, strain weakening is assumed to arise from the alignment of weak basal planes—the development of a crystallographic preferred orientation, CPO—during flow. However, in experiments, ice strain weakening also coincides with grain size reduction, which has been invoked as a weakening mechanism in other minerals. To interrogate the relative contributions of CPO development and grain size reduction toward ice strain weakening, we deformed initially isotropic polycrystalline ice samples to progressively higher strains between -4 and -30°C . Microstructural measurements were subsequently combined with flow laws to separately model the mechanical response expected to arise from CPO development and grain size reduction. Magnitudes of strain weakening predicted by the constitutive flow laws were then compared with the experimental measurements. Flow laws that only consider grain size do not predict weakening with strain despite grain size reduction. In contrast, flow laws solely considering CPO effects can reproduce the measured strain weakening. Thus, it is reasonable to assume that strain weakening in ice is dominated by CPO development, at least under high temperature ($T_h \geq 0.9$) and high stress (>1 MPa), like those in our experiments. We speculate that at high homologous temperatures ($T_h \geq 0.9$), CPO development will also govern the strain weakening behavior of other viscously anisotropic minerals, like olivine and quartz. Overall, we emphasize that geodynamic and glaciological models should incorporate CPOs to account for strain weakening, especially at high homologous temperatures.

Plain Language Summary At high temperatures, ice and other minerals become mechanically weaker during deformation. This “strain weakening” behavior is thought to arise from microscopic processes that reduce grain sizes and align weak lattice planes. Strain weakening is important because it influences the continent-scale flow of rocks and minerals, including terrestrial ice flow. To quantify the relative contributions of grain size reduction and crystal alignment to strain weakening, we deformed ice samples by varying amounts. The microstructure of each sample was then examined using an electron microscope to measure grain size and crystal alignment. These microstructural data were used to predict the strength of each sample using previously published equations (“flow laws”) that link microstructure to sample strength. Model predictions were compared to the measured strength of each sample. We found that very little weakening is predicted due to grain size effects, whereas almost all the observed strain weakening can be accounted for by crystal alignment. Our new results demonstrate that at temperatures approaching a mineral’s melting point—like in polar ice sheets and glaciers—strain weakening is governed by the progressive alignment of weak crystal lattice planes. Models of rock and ice flow should therefore account for both grain size and crystal alignment effects.

1. Introduction

Localized creep deformation of ice within narrow shear margins controls the discharge of terrestrial ice (e.g., Gerbi et al., 2021; Gow & Williamson, 1976; Jansen et al., 2016). To understand large-scale ice dynamics, ice deformation experiments have been used to parameterize the (evolving) strength of polycrystalline ice, for extrapolation to polar conditions (e.g., Azuma, 1995; Durham et al., 1983; Glen, 1955; Goldsby & Kohlstedt, 1997). In laboratory experiments, the creep strength of initially isotropic, polycrystalline ice evolves systematically during deformation (Glen, 1955; Jacka & Maccagnan, 1984; Mellor & Cole, 1982). Strain weakening occurs after secondary

© 2021 The Authors.

This is an open access article under the terms of the [Creative Commons Attribution-NonCommercial License](https://creativecommons.org/licenses/by/4.0/), which permits use, distribution and reproduction in any medium, provided the original work is properly cited and is not used for commercial purposes.

Supervision: David J. Prior, David L. Goldsby
Writing – original draft: Sheng Fan
Writing – review & editing: Sheng Fan, Andrew J. Cross, David J. Prior, Travis F. Hager, Marianne Negrini, Chao Qi

creep (i.e., minimum strain rate) in constant load experiments (Budd & Jacka, 1989; Weertman, 1983), and after peak stress in constant displacement rate experiments (Durham et al., 1983; Fan et al., 2020; Qi et al., 2017; Vaughan et al., 2017). This weakening is often referred to as strain rate “enhancement” in the glaciological and ice sheet literature (Alley, 1992; Budd & Jacka, 1989; Treverrow et al., 2012), and is often accounted for in large-scale ice dynamics models (e.g., Azuma, 1995; Morland & Staroszczyk, 2009; Placidi et al., 2010). Notably, recent work has shown that enhancement must be accounted for in order to accurately infer basal friction—and therefore solid ice discharge—of a flowing ice mass (Rathmann & Lilien, 2021)

Since dislocation glide on the ice basal plane (0001) is at least 60 times easier than glide on any other crystallographic plane (Duval et al., 1983), ice is described as exhibiting strong viscous anisotropy. Due to this anisotropy, ice grains typically rotate to maximize shearing on their basal planes during deformation (Castelnau et al., 1996; Llorens et al., 2016; van der Veen & Whillans, 1994). Furthermore, deformation experiments on ice polycrystals containing a strong, pre-existing CPO show that samples with basal planes favorably aligned for basal slip can deform up to 100 times more easily than samples with basal planes poorly aligned for slip (e.g., Gao & Jacka, 1987; Lile, 1978; Shoji & Langway, 1984, 1988). Thus, many studies of ice sheet dynamics assume that strain rate enhancement (i.e., strain weakening) is caused solely by CPO development (e.g., Azuma, 1994, 1995; Hruby et al., 2020; Morland & Staroszczyk, 2009; Placidi et al., 2010). Accordingly, constitutive ice flow laws are often modified using ad hoc scalar “enhancement factors,” which account for CPO development under specific thermomechanical conditions, loading geometries, and for ice samples with different ages and impurity contents (see review by Cuffey & Paterson, 2010). However, this common assumption—that CPO development governs strain weakening—is largely based on data from uniaxial compression experiments at temperatures above -10°C (Budd & Jacka, 1989; Jacka & Maccagnan, 1984; Li et al., 1996). Under such conditions, ice develops a CPO characterized by a *c*-axis small circle (open cone) around the compression axis, indicating that grains have rotated into weak orientations, favorable for slip on their basal planes. Polar ice sheets and extra-terrestrial cryosphere, on the other hand, can experience ambient temperatures much colder than -10°C (Journaux et al., 2020; Kamb, 2001). Recent experiments have shown that as temperature decreases from -10°C to -30°C , ice *c*-axes instead evolve toward a single cluster parallel with the compression axis (Fan et al., 2020; Fan, Prior, Cross, et al., 2021; Wilson et al., 2019)—a CPO which is unfavorable for easy slip on basal planes. Thus, the role of CPO development in strain weakening may not be straightforward, and CPO development may even lead to strain hardening under certain conditions.

In the study of metals, and minerals other than ice, researchers also invoke grain size reduction as a source of strain weakening (Drury, 2005; McQueen & Jonas, 1975; Rutter, 1999; Sellars, 1978). Grain size reduction arises from the combined operation of dynamic recovery and recrystallization, which remove and reorganize linear defects (i.e., dislocations) into low-energy configurations (Derby & Ashby, 1987; Duval, 1979; Humphreys et al., 2017; Weertman, 1983). By removing defects, and thereby relaxing the internal stress state of grains, recovery and recrystallization can counteract work hardening to produce strain weakening (Derby & Ashby, 1987; Humphreys et al., 2017; Weertman, 1983). Grain size reduction may also produce strain weakening by enhancing grain size sensitive (GSS) creep mechanisms that dominate at fine grain sizes (e.g., grain boundary sliding and diffusion creep; Frost & Ashby, 1982; Raj & Ashby, 1971). In the GSS creep regime, materials become weaker as grain size decreases (Frost & Ashby, 1982). Furthermore, grain rotations during grain boundary sliding—a GSS creep process—are typically thought to weaken pre-existing CPOs (e.g., Bestmann & Prior, 2003; & Skemer, 2017; Warren & Hirth, 2006). Thus, if grain size reduction leads to GSS creep (which promotes strain weakening) with a component of grain boundary sliding (which weakens CPOs), strain weakening may instead be governed by grain size evolution, not CPO development.

Although there are physical rationales, then, for attributing strain weakening to both grain size reduction and CPO development, the relative contributions of these two processes toward enhancement in ice remains unclear. This uncertainty largely arises because CPO development and grain size evolution are strongly coupled; thus, it is difficult to deconvolve their individual and relative effects. Here, we aim to overcome this difficulty by modeling ice strength evolution separately as a function of CPO development and grain size evolution, using microstructure-sensitive constitutive flow laws. In the sections that follow, we first describe the mechanical responses of samples deformed to successively higher strains at temperatures between -30°C and -4°C ($T_h = 0.89\text{--}0.99$). Second, we quantify the microstructure of each deformed sample using cryogenic electron backscatter diffraction (cryo-EBSD; Prior et al., 2015), focusing on measurements of grain size and CPO. Finally, we combine

our microstructural measurements with various ice flow laws (Azuma, 1995; Durham et al., 1983; Glen, 1955; Goldsby & Kohlstedt, 2001) to try and reproduce the experimental ice strength data as a function of strain, using grain size and CPO measurements as model inputs. We compare those modeled stresses and strain rates to the measured (actual) mechanical data to estimate how much of the mechanical response is due to the evolution of grain size and/or CPO under different experimental conditions.

2. Methods

2.1. Experimental Data

2.1.1. Sample Fabrication

Ice samples with controlled initial grain size, random CPO, and minimal porosity were fabricated using a flood-freeze method (Cole, 1979). Details are provided in Fan et al. (2020), Fan, Prior, Cross, et al. (2021), Fan, Prior, Hager, et al. (2021). In brief, we packed sieved ice powders with particle sizes 180–250 μm into cylindrical molds with an internal diameter of 25.4 cm. After that, we flooded the packed molds with degassed ultra-pure deionized water (0°C) under vacuum in a water-ice bath. The flooded molds were then immediately placed vertically on a copper plate for ~ 24 hr at -30°C with polystyrene insulating the cylinders from all the other sides. This step ensures that the freezing front migrates slowly upwards, minimizing the entrapment of bubbles within the samples.

Ice samples, which after freezing had a mean grain size of ~ 300 μm (Fan et al., 2020), were gently pushed out from the molds using an Arbor press. We accidentally also produced medium-grained ice samples, with a mean grain size of ~ 550 μm (Fan, Prior, Cross, et al., 2021), by leaving the frozen, flooded samples in the water-ice bath for ~ 30 min before extraction. The medium-grained ice samples were fabricated with a cylindrical diameter of 27 mm. All samples were cut such that their length was 1.5–2 times their diameter. After cutting, samples were polished on both ends to ensure they were flat and perpendicular to the cylinder axis. After polishing, the initial sample length, L_0 , was measured using a caliper.

2.1.2. Deformation Assembly

Medium-grained ice samples were used for constant load experiments, performed using a 1-atm (unconfined), dead-weight creep apparatus in the Ice Physics Laboratory, University of Otago (Fan, Prior, Cross, et al., 2021). Each ice sample was encapsulated in a rubber jacket together with a walnut wooden platen and a walnut wooden piston (Fan, Prior, Cross, et al., 2021). Encapsulation of the deformation assembly was performed in a -30°C chest freezer. These experiments were conducted at a temperature of $-4 \pm 0.2^\circ\text{C}$, under a constant load of 60 kg, yielding an initial stress of ~ 1.0 MPa (Fan, Prior, Cross, et al., 2021). Experiments were terminated once the true axial strain, ϵ , reached ~ 1 , 4%, 8%, and 13%. We did not apply a stiffness correction to account for elastic deformation of the walnut piston and platen; however, the elastic strain expected in walnut at 1 MPa differential stress is negligible (Appendix A).

Fine-grained ice samples were used for constant displacement rate experiments, performed in a cryogenic tri-axial apparatus (Heard et al., 1990), with a nitrogen gas confining pressure of 20–40 MPa, at $-10 \pm 0.5^\circ\text{C}$ and $-30 \pm 0.5^\circ\text{C}$, in the Ice Physics Laboratory, University of Pennsylvania. Each ice sample was encapsulated in a thin-walled indium jacket tube (~ 0.38 mm wall thickness) with the bottom already welded to a stainless-steel end-cap. The top of indium jacket tube was then welded to a steel semi-internal force gauge, with a thermally insulating zirconia spacer placed between the force gauge and sample. The sample was kept cold in a -60°C ethanol bath during welding. Most of the experiments were conducted under constant uniaxial displacement rates yielding initial strain rates, $\dot{\epsilon}$, of $\sim 1 \times 10^{-5} \text{ s}^{-1}$; these experiments were terminated at strains of $\sim 3\%$, 5%, 8%, 12%, and 20%. Some experiments were also conducted at $-30 \pm 0.5^\circ\text{C}$ with $\dot{\epsilon}$ of $\sim 5 \times 10^{-5} \text{ s}^{-1}$; these experiments were terminated at strains of $\sim 3\%$ and $\sim 20\%$.

2.1.3. Experimental Procedures and Data Processing

All experiments presented in this study were conducted under uniaxial compression loading conditions (Figure 1a). Before the start of each experiment, samples were left to thermally equilibrate with the deformation apparatus for at least 60 min at experiment (pressure, temperature) conditions. After each experimental run, samples were extracted from the apparatus as quickly as possible, before being photographed and measured. To minimize

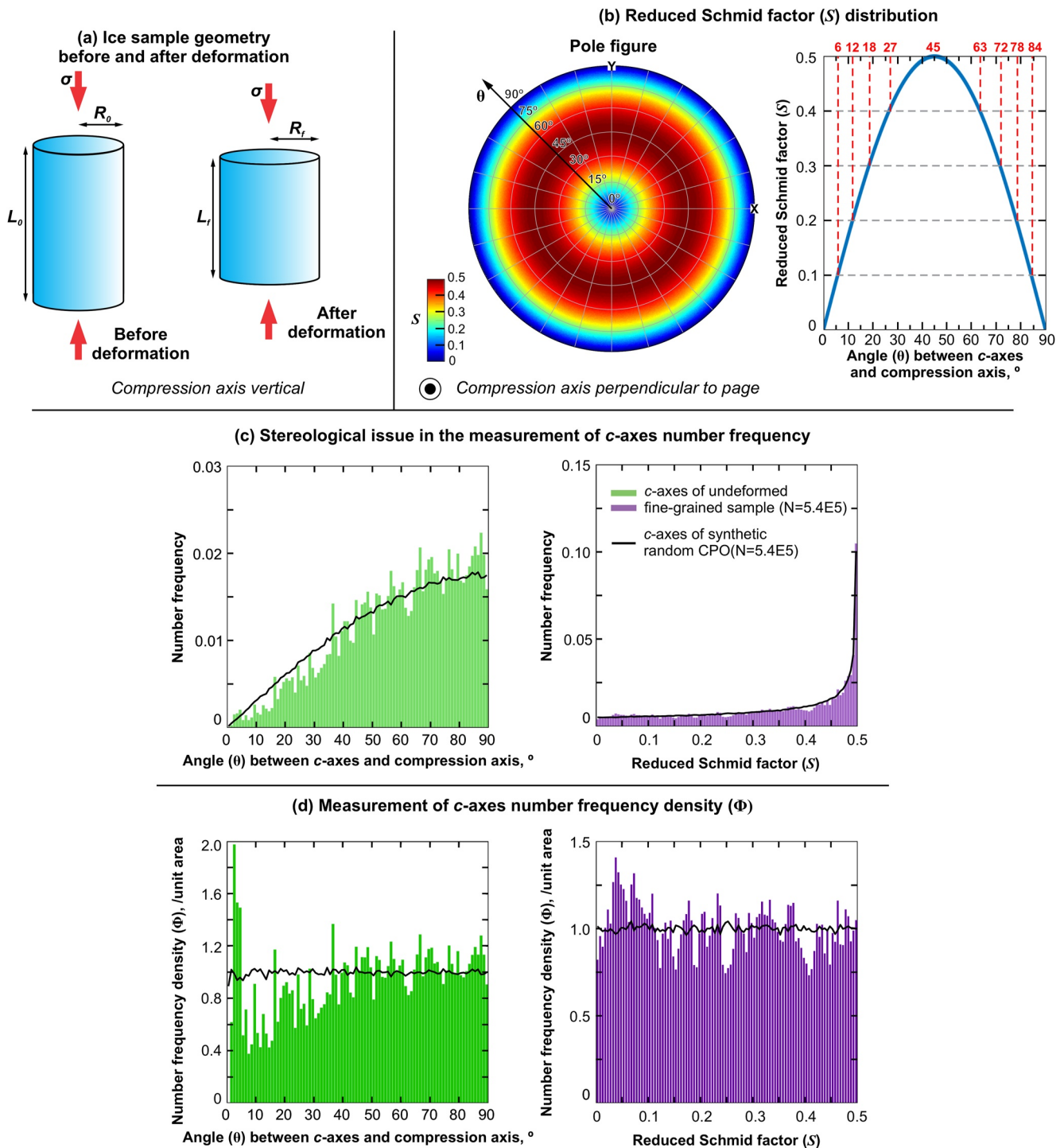


Figure 1. (a) Schematics of ice samples before and after deformation for uniaxial compression. (b) Distribution of reduced Schmid factor, S , as a function of c -axis orientation (Sect. 2.4.2). The left panel shows a pole figure with one million randomly generated c -axis points, colored by their corresponding S value, which is a function of the angle between the c -axis and compression axis, θ (Equation 11). The compression axis is normal to the page. The right panel shows the value of S for c -axes oriented at different angles (θ) from the compression axis. (c) Illustrating the stereological issue in the measurement of c -axis number frequency using the undeformed fine-grained ice sample as an example. Bar plots show the number frequency of measurements at each interval of the angle between c -axes and compression (θ) (colored green) or at each interval of reduced Schmid factor, S (colored purple). (d) Number frequency density, Φ (Section 2.4.2; Appendix D), statistics using the undeformed fine-grained ice sample as an example. Bar plots show Φ of measurements at each interval of the angle between c -axes and compression (θ) (colored green) or at each interval of reduced Schmid factor, S (colored purple). The Black curves represent the distribution of number frequency (c) or number frequency density, Φ (d), for an artificially generated CPO with the same number of points as the undeformed fine-grained ice.

Table 1
Summary of the Mechanical and Grain Size Data for Uniaxial Compression Experiments With Constant Load

Sample no.	T (°C)	ϵ_f	Minimum true axial strain rate		Stress at minimum true axial strain rate		True axial strain at minimum true axial strain rate		Final true axial strain rate	Final stress ^a	Grain number	Grain size parameters (μm)					
			$\dot{\epsilon}_m$ (s^{-1})	σ_m (MPa)	ϵ_m	$\dot{\epsilon}_f$ (s^{-1})	σ_f (MPa)	Peak				Mean	Median	Lower quartile	Higher quartile	Interquartile range (IQR)	
Undeformed	N/A	N/A	N/A	N/A	N/A	N/A	N/A	N/A	N/A	N/A	653	600	535	545	359	730	371
OIL009	-4	0.01	N/A	N/A	N/A	N/A	N/A	1.11×10^{-6}	1.11×10^{-6}	1.02	2,880	357	542	501	340	693	353
OIL008		0.04	Not recorded	Not recorded	Not recorded	Not recorded	Not recorded	1.40×10^{-6b}	1.40×10^{-6b}	0.99	1,716	176	536	453	258	725	467
OIL007		0.08	7.60×10^{-7}	1.01	0.02	0.02	0.02	1.78×10^{-6}	1.78×10^{-6}	0.95	1,569	164	419	411	243	707	464
OIL006		0.13	6.54×10^{-7}	1.01	0.02	0.02	0.02	1.22×10^{-6}	1.22×10^{-6}	0.90	2,309	161	561	337	222	535	313
OIL041		0.13	9.74×10^{-7}	1.01	0.02	0.02	0.02	1.58×10^{-6}	1.58×10^{-6}	0.90							N/A
OIL042		0.13	9.43×10^{-7}	1.01	0.02	0.02	0.02	1.67×10^{-6}	1.67×10^{-6}	0.90							
OIL044		0.13	8.44×10^{-7}	1.01	0.02	0.02	0.02	1.48×10^{-6}	1.48×10^{-6}	0.90							
OIL045		0.13	8.41×10^{-7}	1.01	0.02	0.02	0.02	1.57×10^{-6}	1.57×10^{-6}	0.90							

^aEstimated from load and change of sample cross-sectional area, assuming constant sample volume during the deformation (Equation 3). ^bEstimated from an average of true axial strain rate at 4% strain from experiments with $\epsilon_f \geq 8\%$.

thermal cracking, samples were progressively cooled to ~ -30 , -100 , and then -196°C over a period of ~ 15 min, and were thereafter transferred to a liquid nitrogen dewar for long-term storage. We note that during the time frame of sample extraction, transportation, and preparation for cryo-EBSD, normal grain growth should be negligible (Fan, Prior, Hager, et al., 2021) and significant modifications to CPO are also unlikely (Wilson et al., 2014).

The processed mechanical data are summarized in Tables 1 and 2. During each experimental run, time, t , and vertical shortening of the ice sample, $s(t)$, were recorded every 3–5 s. True axial strain, $\epsilon(t)$, is calculated from the initial ice sample length, L_0 , and piston displacement, $\Delta L(t)$ (Equation 1).

$$\epsilon(t) = -\ln\left(\frac{L_0 - \Delta L(t)}{L_0}\right) \quad (1)$$

The true axial strain rate, $\dot{\epsilon}(t)$, is calculated from the change in true axial strain over the time interval, Δt (Equation 2).

$$\dot{\epsilon}(t) = \frac{\epsilon(t) - \epsilon(t - \Delta t)}{\Delta t} \quad (2)$$

Differential stress, σ , was calculated from the applied axial load, $F(t)$, and cross-sectional area of the ice sample. For constant load experiments, $F(t) = 60 \text{ kg} \times 9.81 \text{ N/kg} = 588.6 \text{ N}$. For constant displacement rate experiments, $F(t)$, was recorded every 3–5 s. Differential stresses have been corrected for the change of sample cross-sectional area during deformation, assuming constant sample volume:

$$\sigma(t) = \frac{F(t)}{\pi R(t)^2}, \quad (3)$$

where $R(t) = R_0 \sqrt{L_0 / (L_0 - \Delta L(t))}$ is the sample radius at time t .

Unless stated otherwise, the term “strain” herein refers to the bulk true axial strain (Equation 1); “strain rate” refers to the true axial strain rate (Equation 2); and “stress” refers to differential stress (Equation 3).

2.2. Microstructural Data

2.2.1. EBSD Data Collection

To quantify grain size distributions and CPOs, we analyzed each sample using cryogenic electron backscatter diffraction (cryo-EBSD). We prepared the ice samples and acquired cryo-EBSD data following the procedures described by Prior et al. (2015). A Zeiss Sigma VP FEG-SEM combined with either an Oxford Instruments NordlysF or Symmetry EBSD camera was used for the data collection (the EBSD camera was upgraded partway through this study). Raw EBSD data were montaged using Oxford Instruments' AZtec software. For fine-grained ice samples, we collected reconnaissance maps with a step size of $30 \mu\text{m}$ from the whole section and, for detailed microstructural analyses, maps with a $5 \mu\text{m}$ step size from selected sub-areas. For medium-grained ice samples, we collected EBSD data with a step size of $30 \mu\text{m}$ from the whole section.

2.2.2. EBSD Data Processing

Ice grains were reconstructed from raw EBSD pixel maps using a Voronoi decomposition algorithm in the MTEX toolbox (Bachmann et al., 2011) with details provided in Fan et al., 2020, Fan, Prior, Cross, et al., 2021, Fan,

Table 2

Summary of the Mechanical and Grain Size Data for Uniaxial Compression Experiments With Constant Displacement Rate

Sample no.	T (°C)	Final true axial strain	Peak stress	True axial strain rate at peak stress	True axial strain at peak stress	Final stress	True axial strain rate at final stress	Grain number	Grain size parameters (μm)					
		ϵ_f	σ_p (MPa)	$\dot{\epsilon}_p$ (s ⁻¹)	ϵ_p	σ_f (MPa)	$\dot{\epsilon}_f$ (s ⁻¹)		Peak	Mean	Median	Lower quartile	Higher quartile	Interquartile range (IQR)
Undeformed	N/A	N/A	N/A	N/A	N/A	N/A	N/A	1,242	300	297	291	165	413	248
PIL176	-10	0.03	1.78	1.03×10^{-5}	0.02	1.70	1.04×10^{-5}	548	29	163	126	52	256	204
PIL163		0.05	2.92	1.03×10^{-5}	0.01	2.42	1.06×10^{-5}	1,282	38	126	98	57	171	114
PIL178		0.08	2.54	1.11×10^{-5}	0.02	1.97	1.19×10^{-5}	894	49	140	118	72	186	114
PIL177		0.12	2.85	1.11×10^{-5}	0.03	1.90	1.21×10^{-5}	1,300	39	115	92	57	154	97
PIL007		0.19	2.13	1.03×10^{-5}	0.02	1.33	1.22×10^{-5}	1,523	37	106	87	51	142	91
PIL165	-30	0.03	8.24	1.08×10^{-5}	0.03	8.15	1.09×10^{-5}	4,923	32	145	103	51	225	174
PIL162		0.05	8.71	1.07×10^{-5}	0.03	7.87	1.10×10^{-5}	2,098	33	105	78	47	136	89
PIL164		0.07	8.93	1.03×10^{-5}	0.03	7.31	1.07×10^{-5}	1,259	31	101	64	41	112	71
PIL166		0.12	7.60	1.11×10^{-5}	0.03	6.45	1.20×10^{-5}	5,447	29	68	55	39	80	41
PIL268		0.21	7.82	1.10×10^{-5}	0.02	5.00	1.31×10^{-5}	6,809	23	62	38	30	56	26
PIL266		0.03	11.29	5.40×10^{-5}	0.03	11.26	5.40×10^{-5}	1,342	36	135	115	53	200	147
PIL243		0.24	10.63	5.40×10^{-5}	0.03	7.35	6.70×10^{-5}	9,259	23	51	39	30	55	25

Prior, Hager, et al., 2021). In brief, grains were defined using a misorientation angle threshold of 10° using the raw EBSD data ($\geq 90\%$ index rate). Data denoising was applied by removing (a) grains with area-equivalent diameter smaller than 20 μm (for maps with 5 μm step size) or 120 μm (for maps with 30 μm step size), (b) grains truncated by the edges of maps, and (3) poorly constrained grains (i.e., grains with <50% indexed pixel coverage). To highlight CPO patterns, contoured pole figures were constructed from the filtered EBSD maps with 30 μm step size, using all indexed pixels and a contouring half-width of 7.5°. Grain size was calculated from the filtered EBSD maps with 5 and 30 μm step size for the fine-grained and medium-grained samples, respectively.

2.3. Mechanical Models

In this study, we attempt to model (i.e., reproduce) the transient evolution of ice strength—that is, the experimental stress-strain and strain rate-strain curves—using ice flow laws that account, separately, for changes in grain size (Goldsby & Kohlstedt, 1997, 2001) and CPO (Azuma, 1994, 1995). We constrain the models using grain sizes and CPOs measured from each experimental sample, representing the microstructural state at increasing finite strains. Strictly speaking, the flow laws used in this study describe the rheological behavior of ice only under steady-state (i.e., strain-invariant) conditions; that is, under conditions where strain rate and stress do not change significantly with increasing strain. Our modeling approach is therefore based on a key assumption that at each infinitesimal strain increment, the ice aggregate deforms at a quasi-steady-state (e.g., Holtzman et al., 2018). Although recent studies (e.g., Soleymani et al., 2020) have found that microstructures take some time to respond to changes in stress and/or strain rate, this lag is generally insignificant under high homologous temperature conditions (Soleymani et al., 2020)—as in our experiments ($T_h = 0.89\text{--}0.99$)—due to rapid recovery and recrystallization (Cross & Skemer, 2019; Fan et al., 2020; Fan, Prior, Cross, et al., 2021; Holtzman et al., 2018).

2.3.1. Mechanical Response Without Microstructural Evolution

As a reference, we calculate the strength predicted by the microstructure-insensitive constitutive flow laws of Glen (1955) and Durham et al. (1983). These flow laws were derived from laboratory experiments on relatively coarse-grained samples, in which creep was assumed to proceed solely via grain size insensitive (GSI) dislocation creep, with no grain size sensitive (GSS) component. These flow laws also do not explicitly account for enhancement due to CPO development. Glen's flow law describes secondary creep, derived using bulk strain rate

Table 3
Parameters of Glen's Flow Law, Durham's Flow Law, and Goldsby-Kohlstedt Composite Flow Law

Name of flow law	Creep regime	n	p	T, temperature	A, material-dependent parameter	Q (Activation energy, kJ/mol) or H (activation enthalpy, kJ/mol)	Reference
Glen's flow law	N/A	3	N/A	$T \geq 263K$	$1.73 \times 10^{21} \text{ (MPa}^{-3}\text{s}^{-1}\text{)}$	$Q = 139$	Kuiper, De Bresser, et al. (2020)
				$T < 263K$	$3.61 \times 10^5 \text{ (MPa}^{-3}\text{s}^{-1}\text{)}$	$Q = 60$	
Durham's flow law	N/A	4	N/A	$T \geq 243K$	$10^{11.8} \text{ (MPa}^{-4}\text{s}^{-1}\text{)}$	$H = 91$	Durham et al. (1983)
Goldsby-Kohlstedt flow law	Dislocation	4	0	$T > 262K$	$6.0 \times 10^{28} \text{ (MPa}^{-4}\text{s}^{-1}\text{)}$	$Q = 181$	Kuiper, Weikusat, et al. (2020), Kuiper, De Bresser, et al. (2020)
				$T < 262K$	$5.0 \times 10^5 \text{ (MPa}^{-4}\text{s}^{-1}\text{)}$	$Q = 60$	
	GBS-limited	1.8	1.4	$T > 262K$	$3.0 \times 10^{26} \text{ (MPa}^{-1.8} \text{ m}^{1.4}\text{s}^{-1}\text{)}$	$Q = 192$	
				$T < 262K$	$3.90 \times 10^{-3} \text{ (MPa}^{-1.8} \text{ m}^{1.4}\text{s}^{-1}\text{)}$	$Q = 49$	

minimum data for ice deformed under constant load (Glen, 1955). In secondary creep, polycrystalline samples retain a nominally random CPO. Durham's flow law, on the other hand, was derived from flow stresses measured at high strains (usually >10% sample shortening) for ice samples deformed in uniaxial compression under constant displacement rates (Durham et al., 1983). Thus, Durham's flow law may implicitly incorporate the mechanical effects of CPO development and grain size, as ice deformed to >10% strain typically undergoes appreciable recrystallization and CPO development (e.g., Fan et al., 2020).

Glen's and Durham's flow laws can be expressed in the general form:

$$\dot{\epsilon} = A\sigma^n \exp\left(-\frac{Q}{RT}\right), \quad (4)$$

where $A \text{ (MPa}^{-n}\text{m}^p\text{s}^{-1}\text{)}$ is a material-dependent parameter, $\sigma \text{ (MPa)}$ is differential stress, n is the stress exponent, $R \text{ (} = 8.314 \times 10^{-3} \text{ kJ mol}^{-1} \text{ K}^{-1}\text{)}$ is the gas constant, and $T \text{ (K)}$ is the absolute temperature. $Q \text{ (kJ mol}^{-1}\text{)}$ is the activation energy for Glen's flow law, and is the activation enthalpy for Durham's flow law. Flow law parameters are summarized in Table 3.

2.3.2. Mechanical Response Due to Evolving Grain Size

From experiments performed on fine-grained water ice, Goldsby and Kohlstedt (2001) proposed a composite flow law in which the total strain rate, $\dot{\epsilon}_{total}$ arises from the strain rate contributions of four distinct creep mechanisms: (a) diffusion creep, $\dot{\epsilon}_{diff}$, (b) grain boundary sliding (GBS) rate-limited by basal slip, $\dot{\epsilon}_{basal}$, (c) basal slip rate-limited by GBS, $\dot{\epsilon}_{GBS}$, and (d) dislocation creep, $\dot{\epsilon}_{dist}$:

$$\dot{\epsilon}_{total} = \dot{\epsilon}_{diff} + \left(\frac{1}{\dot{\epsilon}_{basal}} + \frac{1}{\dot{\epsilon}_{GBS}}\right)^{-1} + \dot{\epsilon}_{dist} \quad (5)$$

The term $(1/\dot{\epsilon}_{basal} + 1/\dot{\epsilon}_{GBS})^{-1}$ represents the serial operation of basal slip and GBS as accommodation mechanisms—the slower of these two processes limits their combined strain rate. At temperatures warmer than 220 K, and stresses greater than 10^{-4} MPa, $\dot{\epsilon}_{diff}$ and $\dot{\epsilon}_{basal}$ will be negligible for grain sizes greater than 1 mm (Goldsby, 2006). Thus, we can apply the composite flow law in a simplified form:

$$\dot{\epsilon}_{total} = \dot{\epsilon}_{dist} + \dot{\epsilon}_{GBS} \quad (6)$$

Dislocation creep is a grain size insensitive mechanism described by a constitutive equation of the form shown in Equation 4. GBS, on the other hand, is a grain size sensitive mechanism:

$$\dot{\epsilon} = A\sigma^n d^{-p} \exp\left(-\frac{Q}{RT}\right), \quad (7)$$

where d is grain size (m), and p is the grain-size exponent. Goldsby and Kohlstedt (1997, 2001) derived $n = 4$ for dislocation creep (at high stresses) and $n = 1.8$ for GBS (at low stresses) and proposed that Glen's law ($n \approx 3$) arises from roughly equal contributions of dislocation creep and GBS at intermediate stresses. Recent glaciological

modeling by Behn et al. (2020) likewise suggests that combined dislocation creep and GBS produces an apparent stress exponent of $n = 3$ for ice sheets. We use the simplified composite flow law (Equation 6)—hereafter referred to as the “grain-size-sensitive model”—to estimate ice strength evolution arising from grain size evolution, using the revised composite flow law parameters provided in Table 3 (Kuiper, De Bresser, et al., 2020; Kuiper, Weikusat, et al., 2020).

2.3.3. Mechanical Response Due to Evolving CPO

To account for evolving viscous anisotropy (and enhancement) due to CPO development, Azuma (1994, 1995) developed a power law model that describes the creep strength of polycrystalline ice as a function of the total shear stress resolved onto (weak) ice basal planes. Azuma's flow law introduces the parameter S_{mean} —a scalar term which represents the average reduced basal Schmid factor, S , for a given grain population. For each crystallographic orientation, the reduced basal Schmid factor, S , reflects the amount of shear stress resolved onto the basal plane (i.e., the easy glide plane); note that this does not account for the amount of shear stress resolved along a particular Burgers vector (slip direction) lying within the basal plane. In short, S_{mean} can be considered a proxy for the total shear stress resolved on ice basal planes in a polycrystal. Azuma's flow law takes a similar form to that given in Equation 4:

$$\dot{\epsilon} = B\sigma^n \exp\left(-\frac{Q}{RT}\right) \quad (8)$$

However, the pre-exponential term, B ($MPa^{-n}s^{-1}$) follows a power law relationship with S_{mean} (see Figure 9 from Azuma, 1995):

$$B \propto S_{mean}^q, \text{ where } q \approx 4 \quad (9)$$

such that, at a given stress, an ice sample with more shear stress resolved on basal planes (i.e., large S_{mean}) will deform faster than an ice sample with little shear stress resolved on basal planes (i.e., small S_{mean}).

Azuma's model makes the key assumption that under their experimental conditions—relatively low temperatures (-10 to -20°C), low strain rates ($\sim 2 \times 10^{-7}$ to $4 \times 10^{-7} s^{-1}$), and low strains ($\sim 5.7\%$)—dynamic recrystallization should be negligible. Thus, all strain weakening measured in their experiments is attributed to CPO development. However, Azuma (1995) also observed that for a given value of S_{mean} , small variations in B could be attributed to differences in grain size, impurity content, and grain shape among different experimental studies. In this study, we place upper and lower bounds on B — B_{upper} and B_{lower} , respectively—for each S_{mean} value, following Figure 9 from Azuma (1995).

$$\log_{10}(B_{upper}) = 4.2 \cdot \log_{10}(S_{mean}) + 8 \quad (10)$$

$$\log_{10}(B_{lower}) = 4.8 \cdot \log_{10}(S_{mean}) + 7.4$$

In this study, we use Azuma's (1994, 1995) model—herein termed the “CPO-only model”—to model ice strength evolution arising from CPO development alone, following Equations 8–10.

2.4. Model Input Data

To reiterate, we use grain sizes and c -axis orientations calculated from EBSD maps (Section 2.2) of ice samples deformed to successively higher strains (Section 2.1) as an input to the constitutive relationships described above (Section 2.3), along with the experimental boundary conditions (temperature, stress, and/or strain rate). These models are then used to estimate the contributions of grain size evolution and CPO development to bulk strain weakening.

2.4.1. Grain Size

Grain size is defined here as the diameter of a circle with an area equal to the measured area of each grain (i.e., area-equivalent diameter). We use both median grain size and the full grain size distribution of each sample as an input into the grain-size-sensitive model (Equation 6). Median grain sizes have been shown to most accurately

reflect the “average” grain size of right-skewed and lognormal grain size distributions (Lopez-Sanchez, 2020; Ranalli, 1984) like those observed in our samples (Fan et al., 2020; Fan, Prior, Cross, et al., 2021).

To model ice strength evolution using full grain size distributions, we first estimate the volume fraction of different grain size classes using the Scheil-Schwartz-Saltikov method (Saltikov, 1967; Scheil, 1931; Schwartz, 1934) (details in Appendix B). For polycrystalline materials, aggregate strength falls between two end-member bounds: (a) a homogeneous stress bound (Sachs bound), with local strain rate varying from grain to grain, and (b) a homogeneous strain rate bound (Taylor bound), with local stress varying from grain to grain (Freeman & Ferguson, 1986; Ter Heege et al., 2004). In reality, aggregate strength should fall between these end-member bounds (Tullis et al., 1991). To place upper and lower bounds on sample strength evolution, we thus calculate both the Sachs and Taylor limits for each experimental sample (details in Appendix C). It is worth noting here that the composite flow law (Goldsby & Kohlstedt, 1997, 2001)—which forms the basis of the grain-size-sensitive model here—was derived from fine-grained (<100 μm) ice samples deformed at low temperatures ($\leq -25^{\circ}\text{C}$), to low strains (mostly $\leq 3\%$). We assume that Goldsby & Kohlstedt's samples did not undergo significant grain size reduction, meaning that their composite flow law reflects the strength of ice with a nominally monodisperse grain size distribution. In other words, the grain-size-sensitive models should not already incorporate implicit grain size distribution effects.

2.4.2. Crystallographic Preferred Orientation (CPO)

For each sample, *c*-axis orientations measured via EBSD (one point per pixel) were used to estimate the amount of shear stress resolved on crystallographic basal planes, quantified using the reduced Schmid factor, *S* (e.g., Azuma, 1995). Under uniaxial compression, where the compression direction is parallel to the sample shortening axis (Figure 1a), *S* can be calculated from the angle (θ) between each *c*-axis measurement and the compression axis (Equation 11):

$$S = \frac{\sin(2\theta)}{2} \quad (11)$$

S is highest (value of 0.5) for *c*-axes oriented 45° from the compression direction, and decreases to zero as *c*-axes become parallel or perpendicular to the compression direction.

The number frequency of *c*-axes observed from a 2-D surface is impacted by a stereological issue that, in turn, biases reduced Schmid factor measurements. Namely, for a random orientation distribution, *c*-axes lying sub-normal to the compression direction ($\theta \approx 90^{\circ}$) are much more abundant than *c*-axes lying sub-parallel to the compression direction ($\theta \approx 0^{\circ}$; see Figure 1c, green histogram). This effect arises because the area of a stereoplot lying between two “co-latitudes” (i.e., small circles) of fixed separation (e.g., 10°) increases with increasing angle (θ) from the stereoplot center (Figure 1b). For a random population of *c*-axes, this effect produces a reduced Schmid factor frequency distribution that is strongly biased toward high reduced Schmid factors (purple histogram, Figure 1c). However, for a random orientation distribution, the densities (number frequency per unit area) of *c*-axes lying between two co-latitudes of fixed separation should be the same (Figure 1d; details for the calculation of *c*-axis densities are in Appendix D). Consequently, there should be a uniform density distribution of reduced Schmid factors for a random orientation distribution (Figure 1d). To account for this issue, we can normalize the bulk reduced Schmid factor, S_{bulk} , following:

$$S_{bulk} = \frac{\Phi_1 \bar{S}_1 + \Phi_2 \bar{S}_2 + \Phi_3 \bar{S}_3 + \dots + \Phi_m \bar{S}_m}{\Phi_1 + \Phi_2 + \Phi_3 + \dots + \Phi_m}, \quad (12)$$

where $\bar{S}_1, \bar{S}_2, \bar{S}_3, \dots, \bar{S}_m$ are the mean values of reduced Schmid factor in each of *m* classes of reduced Schmid factors ($S_1, S_2, S_3, \dots, S_m$) and number frequency densities ($\Phi_1, \Phi_2, \Phi_3, \dots, \Phi_m$). Here, we use 100 classes (bins) of reduced Schmid factors (i.e., $m = 100$; Schmid factor interval of 0.005). However, there is very little difference between ice strengths modeled using the normalized and unnormalized reduced Schmid factor values (Section S1 of Supporting Information S1). For simplicity, we herein discuss only the models that use normalized Schmid factor values.

2.5. Normalization of Measured and Modeled Bulk Strain Rate/Stress

To assess how well each model reproduces the measured (experimental) mechanical data, we need to examine both (a) the absolute magnitude of the stresses and strain rates predicted by each model and (b) the “patterns” of strain

Table 4
Summary of Measured and Estimated Strain Rate for Experiments With Constant Load at -4°C

Sample no.	T ($^{\circ}\text{C}$)	Initial stress (MPa)	Measured minimum strain rate (s^{-1})	Measured strain rate at maximum strain, absolute (s^{-1})/normalised	Estimated strain rate, absolute (s^{-1})/normalised		Grain-size-sensitive model (simplified Goldsby-Kohlstedt composite flow law)		Bulk reduced Schmid factor, S_{bulk}	Estimated strain rate, absolute (s^{-1})/normalised	
					Glen's flow law	Durham's flow law	Strain rate estimated from grain size distribution, absolute (s^{-1})/normalised	Strain rate estimated from median grain size, absolute (s^{-1})/normalised		With upper bound of \mathbf{A}	With lower bound of \mathbf{B}
Undeformed medium-grained	N/A	N/A	N/A	N/A	N/A	N/A	N/A	N/A	0.2449	N/A	N/A
OIL009	-4	~ 1	N/A	$1.11 \times 10^{-6}/1.00$	$1.80 \times 10^{-6}/1.00$	/1.00	$7.63 \times 10^{-7}/1.00$	$1.10 \times 10^{-6}/1.00$	0.2514	$6.92 \times 10^{-7}/1.00$	$7.59 \times 10^{-8}/1.00$
OIL008			Not recorded	Not recorded	$1.70 \times 10^{-6}/0.94$	$1.28 \times 10^{-6}/0.92$	$6.37 \times 10^{-7}/0.83$	$1.20 \times 10^{-6}/1.09$	0.3239	$2.01 \times 10^{-6}/2.90$	$2.56 \times 10^{-7}/3.37$
OIL007			7.60×10^{-7}	$1.78 \times 10^{-6}/2.34$	$1.49 \times 10^{-6}/0.82$	$1.07 \times 10^{-6}/0.77$	$6.14 \times 10^{-7}/0.80$	$1.30 \times 10^{-6}/1.19$	0.3295	$2.16 \times 10^{-6}/3.12$	$2.78 \times 10^{-7}/3.66$
OIL006			6.54×10^{-7}	$1.22 \times 10^{-6}/1.87$	$1.30 \times 10^{-6}/0.72$	$9.01 \times 10^{-7}/0.65$	$7.50 \times 10^{-7}/0.98$	$1.60 \times 10^{-6}/1.45$	0.3766	$3.78 \times 10^{-6}/5.46$	$5.28 \times 10^{-7}/6.96$

^aA pre-exponential term, which generally has a power law relationship with S_{bulk} (Equation 10).

weakening predicted by each model—that is, the relative amount (percentage) of strain weakening predicted by each model, and the predicted strains required to reach steady-state conditions. To make it easier to assess the patterns of strain weakening predicted by each model, we normalize the modeled and measured stresses (for constant displacement rate experiments) and strain rates (for constant load experiments) by their values at the strain corresponding most closely to the peak stress and minimum strain rate, respectively. This method is similar to that applied by Jacka and Li (2000) and enables us to make a more direct comparison between the patterns of strain weakening predicted by each model, while also removing sample-to-sample variability. Meanwhile, the unnormalized data are used to assess how well each model reproduces the absolute measured stress and strain rate magnitudes. The unnormalized and normalized mechanical data are summarized for each sample in Tables 4–6.

2.5.1. Constant Load Experiments

For each experimental run with constant load, the measured strain rate-strain curves are normalised with respect to the minimum strain rate following:

$$\bar{\dot{\epsilon}}_{\text{measure}} = \frac{\dot{\epsilon}_{\text{measure}}}{\dot{\epsilon}_{\text{min,measure}}}, \quad (13)$$

where $\bar{\dot{\epsilon}}_{\text{measure}}$ is the normalised measured strain rate, $\dot{\epsilon}_{\text{min,measure}}$ is the measured minimum strain rate at ~ 1 – 2% strain.

Modeled uniaxial strain rates were normalised following:

$$\bar{\dot{\epsilon}}_{\text{model}} = \frac{\dot{\epsilon}_{\text{model}}}{\dot{\epsilon}_{1\%,\text{model}}}, \quad (14)$$

where $\bar{\dot{\epsilon}}_{\text{model}}$ is the normalised modeled strain rate, $\dot{\epsilon}_{\text{model}}$ is the modeled strain rate corresponding to the maximum strain of each sample, $\dot{\epsilon}_{1\%,\text{model}}$ is the modeled strain rate at the strain of $\sim 1\%$.

2.5.2. Constant Displacement Rate Experiments

For each experimental run with constant displacement rate, the measured stress-strain curves are normalised with respect to the peak stress following:

$$\bar{\sigma}_{\text{measure}} = \frac{\sigma_{\text{measure}}}{\sigma_{\text{peak,measure}}}, \quad (15)$$

where $\bar{\sigma}_{\text{measure}}$ is the normalised measured stress, $\sigma_{\text{peak,measure}}$ is the measured uniaxial stress at $\sim 2\%$ – 3% strain. The decrease of normalised measured stress relative to the peak, $\Delta\bar{\sigma}_{\text{measure}}$, is:

$$\Delta\bar{\sigma}_{\text{measure}} = 1 - \bar{\sigma}_{\text{measure}} \quad (16)$$

Modeled stresses are normalised for ice samples deformed under the same temperature and similar strain rates following:

$$\bar{\sigma}_{\text{model}} = \frac{\sigma_{\text{model}}}{\sigma_{3\%,\text{model}}}, \quad (17)$$

where $\bar{\sigma}_{\text{model}}$ is the normalised modeled stress, σ_{model} is the modeled stress corresponding to the maximum strain of each sample, $\sigma_{3\%,\text{model}}$ is the modeled stress at the strain of $\sim 3\%$. At each finite strain, the decrease of normalised modeled stress relative to 3% strain, $\Delta\bar{\sigma}_{\text{model}}$, is:

Table 5
Summary of Measured and Estimated Stress for Experiments With Constant Displacement Rate at -10°C

Sample no.	T ($^{\circ}\text{C}$)	Initial strain rate (s^{-1})	Measured peak stress (MPa)	Measured stress at maximum strain, absolute (MPa)/normalised	Estimated stress, absolute (MPa)/normalised		Grain-size-sensitive model (simplified Goldsby-Kohlstedt composite flow law)			Estimated stress, absolute (MPa)/normalised	
					Microstructure-insensitive models		Stress estimated from grain size distribution, absolute (MPa)/normalised	Stress estimated from median grain size, absolute (MPa)/normalised	Bulk reduced Schmid factor, S_{bulk}	CPO-only model (Azuma's flow law)	
					Glen's flow	Durham's flow				With upper bound of B	With lower bound of B
Undeformed standard ice	N/A	N/A	N/A	N/A	N/A	N/A	N/A	N/A	0.2438	N/A	N/A
PIL176	-10	$\sim 1 \times 10^{-5}$	1.78	1.70/0.96	2.90/1.00	2.10/1.00	3.39/1.00	3.03/1.00	0.2620	2.88/1.00	5.96/1.00
PIL163			2.92	2.42/0.83	2.92/1.01	2.11/1.00	3.35/0.99	2.88/0.95	0.2866	2.55/0.89	5.20/0.87
PIL178			2.54	1.97/0.78	3.03/1.04	2.17/1.03	3.47/1.03	3.13/1.03	0.3516	1.99/0.69	3.90/0.65
PIL177			2.85	1.90/0.67	3.05/1.05	2.18/1.04	3.45/1.02	2.96/0.97	0.3250	2.24/0.78	4.44/0.75
PIL007			2.13	1.33/0.62	3.06/1.06	2.19/1.04	3.42/1.01	3.08/1.02	0.3898	1.74/0.60	3.33/0.56

$$\Delta \bar{\sigma}_{\text{model}} = 1 - \bar{\sigma}_{\text{model}} \quad (18)$$

3. Results

3.1. Measured Mechanical Data

3.1.1. Constant Load Experiments

The measured strain rate, $\dot{\epsilon}_{\text{measure}}$, and normalised strain rate, $\bar{\epsilon}_{\text{measure}}$, data are plotted as a function of strain in Figures 2a–2c and 3a–3c, respectively (black curves). Measured and normalised strain rates initially decrease with strain before reaching a minimum at $\sim 1\%$ – 2% shortening. After that, deformation accelerates until a nominally steady-state strain rate is reached at around $\epsilon = \sim 6\%$. However, in many experiments there is a slight strain rate decrease beyond $\epsilon = \sim 8\%$. Meanwhile, stress decreases modestly during each constant load experiment, due to an increase in sample cross-sectional area (black line, Figure 2d; Equation 3).

3.1.2. Constant Displacement Rate Experiments

Measured stresses are plotted as a function of strain in Figures 2e–2g, 2i–2k, and 2m–2o (black curves). Stress initially increases as a function of strain, reaching a peak at strains of 1% – 3% . Thereafter, stress drops 31% – 38% until a flow stress is reached by $\sim 20\%$ shortening (black curves, Figures 3e–3g, 3i–3k, and 3m–3o; black dots, Figures 3h, 3l, and 3p; Tables 5 and 6). In general, both peak and flow stresses increase with increasing strain rate and decreasing temperature. Strain rate increases modestly through each constant rate experiment as a result of continuous sample shortening (black lines, Figures 2h, 2l, and 2p; Equation 2).

3.2. Microstructures

The microstructures of these samples have been described in detail in Fan et al. (2020), Fan, Prior, Cross, et al. (2021). We will summarize the pertinent observations here, but the reader can refer to Fan et al. (2020), Fan, Prior, Cross, et al. (2021) for the full details.

Table 6

Summary of Measured and Estimated Bulk Stress for Experiments With Constant Displacement Rate at -30°C

Sample no.	T ($^{\circ}\text{C}$)	Initial strain rate (s^{-1})	Measured peak stress (MPa)	Measured stress at maximum strain, absolute (MPa)/normalised	Estimated stress, absolute (MPa)/normalised		Grain-size-sensitive model (simplified Goldsby-Kohlstedt composite flow law)			Estimated stress, absolute (MPa)/normalised	
					Microstructure-insensitive models		Stress estimated from grain size distribution, absolute (MPa)/normalised	Stress estimated from median grain size, absolute (MPa)/normalised	Bulk reduced Schmid factor, S_{bulk}	CPO-only model (Azuma's flow law)	
					Glen's flow law	Durham's flow law				With upper bound of B	With lower bound of B
PIL165	-30	$\sim 1 \times 10^{-5}$	8.24	8.15/0.99	6.20/1.00	5.01/1.00	5.93/1.00	5.81/1.00	0.2443	6.84/1.00	14.38/1.00
PIL162			8.71	7.87/0.90	6.22/1.00	5.02/1.00	5.92/1.00	5.76/0.99	0.2600	6.29/0.92	13.06/0.91
PIL164			8.93	7.31/0.84	6.16/0.99	4.99/1.00	5.89/0.99	5.64/0.97	0.2742	5.79/0.85	11.88/0.83
PIL166			7.60	6.45/0.85	6.41/1.03	5.13/1.02	6.01/1.01	5.77/0.99	0.2821	5.78/0.84	11.80/0.82
PIL268			7.82	5.00/0.64	6.60/1.06	5.25/1.05	6.19/1.05	5.70/0.99	0.3040	5.36/0.78	10.78/0.75
PIL266	-30	$\sim 5 \times 10^{-5}$	11.29	11.26/1.00	10.57/1.00	7.47/1.00	8.86/1.00	8.81/1.00	0.2586	10.78/1.00	22.38/1.00
PIL243			10.63	7.35/0.69	11.36/1.07	7.89/1.06	9.32/1.05	9.05/1.03	0.3010	9.37/0.87	18.88/0.84

3.2.1. Grain Size

At all temperatures, and at strains higher than $\sim 3\%$, large grains (typically $>150 \mu\text{m}$ in diameter) develop irregular, interlocking grain boundaries. Meanwhile, with increasing strain, networks of fine grains develop along the boundaries of the large, original grains, forming a “core-and-mantle” type structure (Figures 4a–6a). Fine grains become increasingly abundant at the expense of large, original grains, leading to a modest decrease in median grain sizes with increasing strain (Figures 4b–6b and Tables 1 and 2). However, fine grains are volumetrically dominant only in the largest strain ($\geq 12\%$), lowest temperature (-30°C) samples (Figure 6c). In all other samples, large grains occupy a much greater volume of each sample (Figures 4c–6c).

3.2.2. Crystallographic Preferred Orientations (CPOs) and Reduced Schmid Factors

For samples deformed at -4 and -10°C , CPOs are close to random at strains of $\epsilon < \sim 3\%$ (Figures 4d, 4e, 5d, and 5e). CPO patterns become clearer at $\epsilon > \sim 4\%$, with c -axes preferentially aligned in a cone (small circle) centered around the compression axis (Figures 4d and 5d). Accordingly, the number frequency density (Φ , Section 2.4.2) of c -axes at θ of 30 – 50° increases (relative to the undeformed starting material), while Φ decreases for c -axes at $\theta = 0$ – 30° and 50 – 90° —this change becomes more marked with increasing strain (Figures 4e and 5e, gold histograms). For samples deformed at -30°C , the CPO is likewise close to random at small strains ($\leq \sim 5\%$; Figures 6d and 6e). However, with increasing strain ($\epsilon \geq \sim 8\%$), c -axes form a tight cone around the compression axis, increasing the number frequency density of c -axes at 0 – 45° , relative to those at 45 – 90° (Figure 6e, gold histograms). The c -axis cone becomes tighter with increasing strain, until it becomes a single, broad cluster by $\sim 20\%$ strain (Figure 6d).

In all samples with $\epsilon \geq \sim 5\%$, the number frequency density Φ of orientations with $S > 0.4$ increases with strain, regardless of whether c -axes evolve toward an open cone (easy slip) or single broad maxima (hard slip) CPO. Nevertheless, this trend is more pronounced at higher temperatures (-4 and -10°C) that favor open cone (easy slip) CPO development (compare Figures 4f and 5f with Figure 6f). As a result, bulk reduced Schmid factors, S_{bulk} , generally increase with increasing strain, at both high and low temperatures, indicating that sample grain populations evolve toward orientations favorable for bulk easy slip.

Absolute values of experimental measurements and modelling results

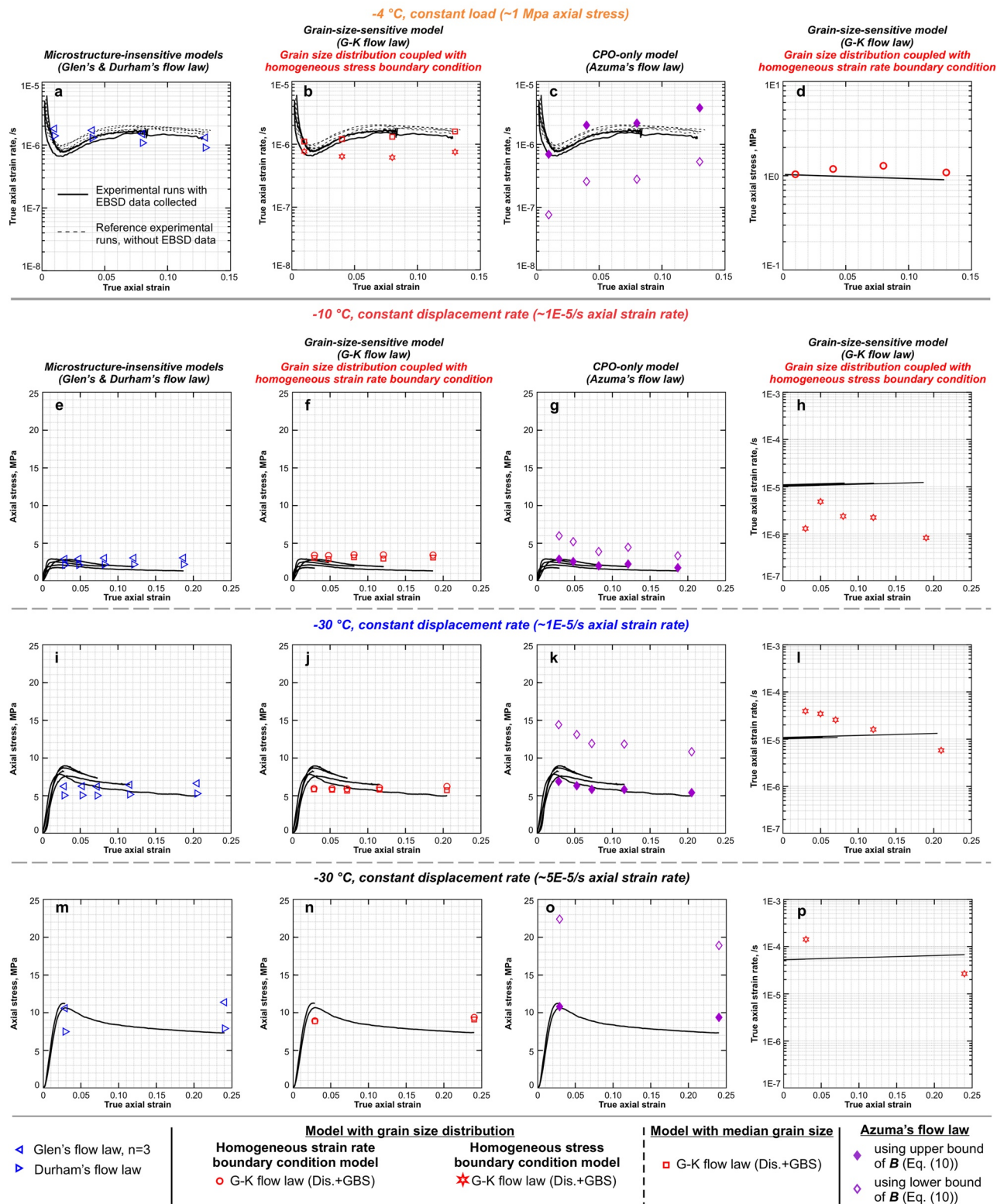


Figure 2.

3.3. Ice Strength Evolution Models

As described above (Sections 2.3 and 2.5), we compare the magnitude (absolute value; Figure 2) and pattern (normalised value; Figure 3) of ice strength evolution between experimental measurements (black curves) and modeling results (colored symbols). For experiments conducted at similar conditions (temperature, stress/strain rate), we model the evolution of strain rate and/or stress as a function of strain and microstructural evolution (grain size, CPO) using:

1. Ice flow laws that do not consider grain size or CPO effects (Durham et al., 1983; Glen, 1955) (blue symbols, first column in Figures 2 and 3). These form the basis of our so-called “microstructure-insensitive models.”
2. An ice flow law that incorporates grain size sensitivity but not CPO development (Goldsby & Kohlstedt, 1997, 2001). This forms the basis of our so-called “grain-size-sensitive models.” We account for grain size evolution using both median grain sizes (red squares, second column in Figures 2 and 3) and the full measured grain size distributions. For models that use the full grain size distribution, we calculate both the isostrain (Sachs) limit (red circles) and isostrain (Taylor) limit (red stars).
3. An ice flow law that accounts for CPO development but not grain size evolution (Azuma, 1994, 1995) (purple symbols, third column in Figures 2 and 3). This forms the basis of our so-called “CPO-only model.”

3.3.1. The Magnitude (Absolute Value) of Strain Rate or Stress

At all conditions, the mechanical models (colored symbols, Figures 2 and 3) all predict ice strengths within an order of magnitude of those measured experimentally (black curves, Figures 2 and 3). The grain-size-sensitive models show similar results regardless of whether median grain sizes and or the full grain size distributions are used (red symbols, second column in Figure 2). These models are also very similar to the microstructure-insensitive (Glen, Durham) models (compare first and second columns in Figure 2). Both types of model predict strain rates that lie between the measured secondary minimum and tertiary maximum strain rates for constant load experiments (Figures 2a and 2b), and stresses that lie between the measured peak and flow stresses for constant displacement rate experiments (Figures 2e–2f, 2i–2j, and 2m–2n). For the CPO-only model (Azuma, 1994, 1995), the strain rates (for constant load experiments) and stresses (for constant displacement rate experiments) predicted using the upper bound of the pre-exponential term, B (Equation 9, Section 2.3.3) lie very close to the experimental measurements (Figures 2c, 2g, 2k, and 2o).

3.3.2. The Pattern (Normalised Value) of Strain Rate or Stress

The microstructure-insensitive models (colored blue) and grain-size-sensitive models (colored red) estimate that sample strength does not evolve significantly as a function of strain (Figures 3a–3b, 3e–3f, 3i–3j, and 3m–3n). Such a prediction does not match the experimental measurements—normalised strain rate increases with strain after secondary minimum (under constant load); normalised stress decreases with strain after peak stress (black curve, Figure 3).

Meanwhile, the CPO-only model closely matches the measured magnitudes of strain weakening in most cases (Figures 3c, 3g, 3k, and 3o). However, the CPO-only model overestimates the strain rate increase under constant load conditions (at -4°C) by a factor of ~ 3 (Figures 3c and 3d), and underestimates the stress drop magnitude by a factor of ~ 2 under constant displacement rate conditions at -30°C and $\sim 5 \times 10^{-5} \text{ s}^{-1}$ strain rate (Figures 3o and 3p). The model also predicts that, at lower temperatures, strain weakening is less pronounced (compare Figures 3g and 3h with Figures 3k–3l and 3o–3p).

Figure 2. Comparing the absolute values of measured and modeled mechanical data for experiments under conditions of: (a)–(d) constant load ($\sigma = \sim 1 \text{ MPa}$), $T = -4^{\circ}\text{C}$; (e)–(h) constant displacement rate ($\dot{\epsilon} = \sim 1 \times 10^{-5} \text{ s}^{-1}$), $T = -10^{\circ}\text{C}$; (i)–(l) constant displacement rate ($\dot{\epsilon} = \sim 1 \times 10^{-5} \text{ s}^{-1}$), $T = -30^{\circ}\text{C}$; (m)–(p) constant displacement rate ($\dot{\epsilon} = \sim 5 \times 10^{-5} \text{ s}^{-1}$), $T = -30^{\circ}\text{C}$. Mechanical data from experimental measurements are colored black; Modeled mechanical data are colored non-black. Sample strengths predicted by the microstructure-insensitive mechanical models (Section 2.3.1) are illustrated in (a), (e), (i) and (m). Sample strengths predicted by the grain-size-sensitive model (Section 2.3.2) are shown in (b), (f), (j) and (n). Sample strengths predicted by the CPO-only model (Section 2.3.3) are shown in (c), (g), (k) and (o). For models that incorporate the full grain size distribution, we calculate both the homogeneous stress (Sachs bound) boundary condition (a–c, h, l, p), and the homogeneous strain rate (Taylor bound) boundary condition (d, e–g, i–k, m–o).

Normalised values of experimental measurements and modelling results

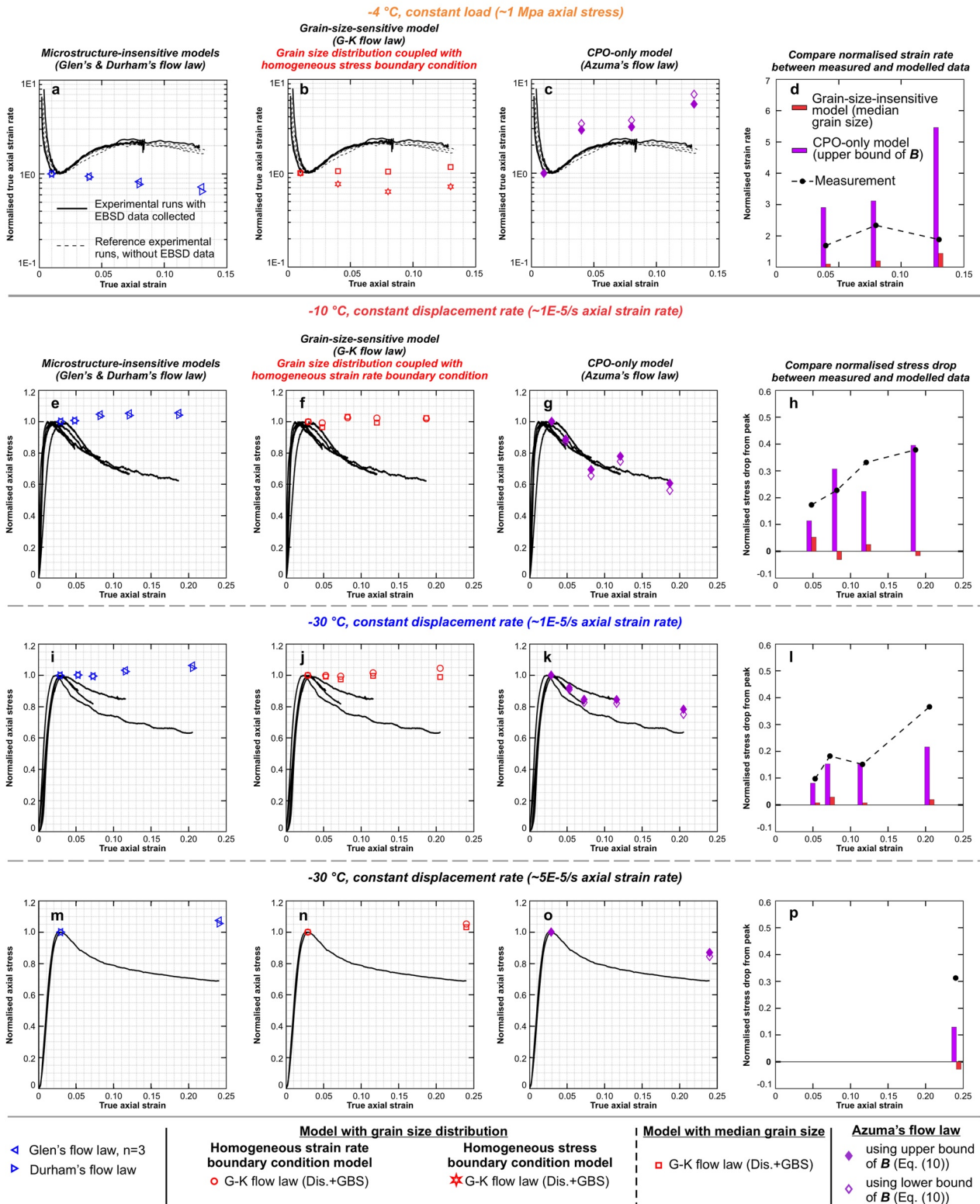


Figure 3.

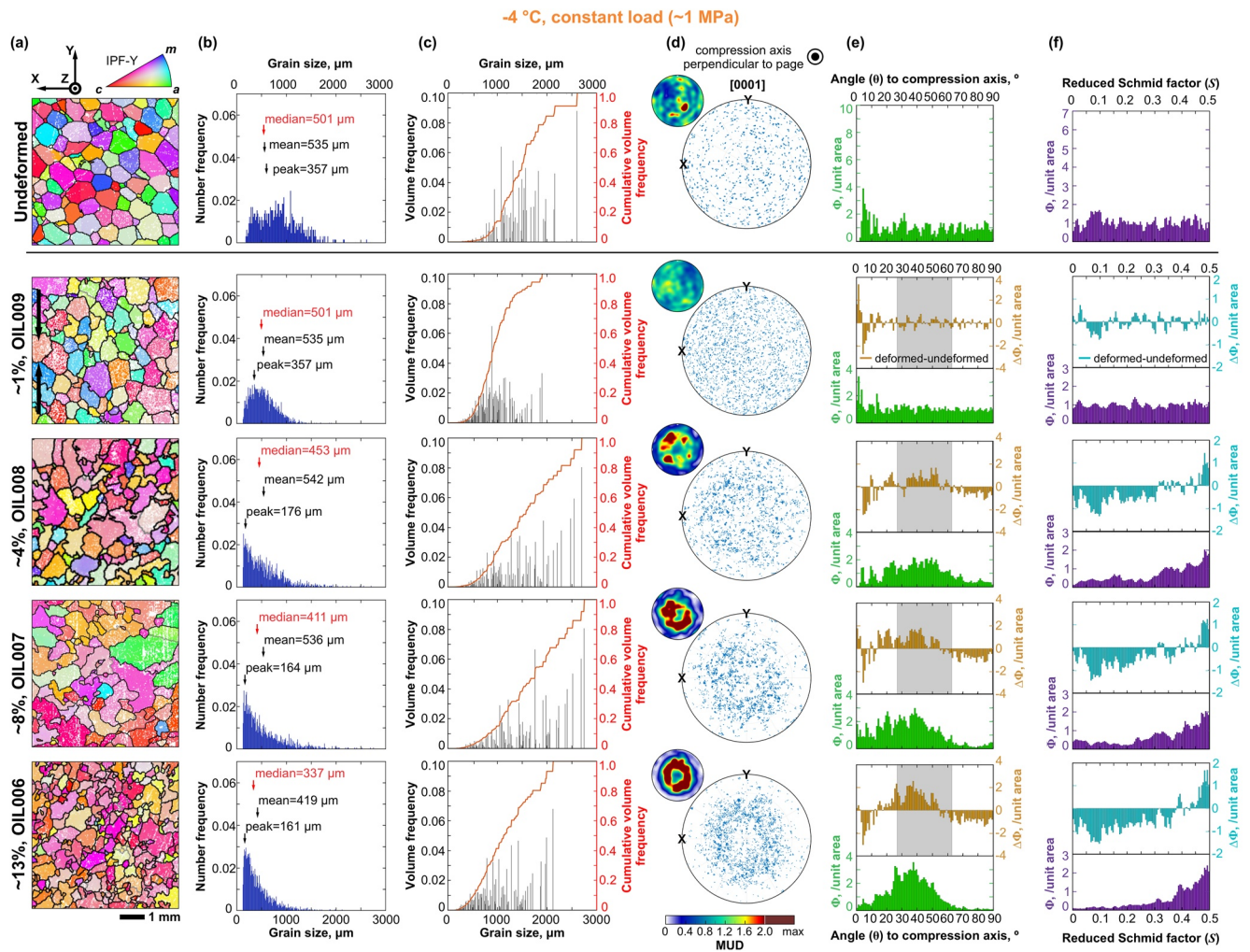


Figure 4. Microstructural analyses of deformed ice samples at -4°C under uniaxial compression with constant load ($\sigma \approx 1$ MPa). The EBSD data are presented as (a) orientation maps. Orientation maps are colored by IPF-Y, where colors indicate which crystallographic axes are parallel to the vertical shortening direction, as shown by the black arrows. Ice grain boundaries with a misorientation larger than 10° are shown black. Non-indexed pixels are shown white. Subgrain boundaries, where misorientation angles between neighboring pixels are between 2° and 10° , are shown in gray. Maps show data without pixel interpolation. (b) Grain size distribution with a bin width of $10\ \mu\text{m}$ for each grain size class. Mean and peak grain sizes are indicated by black arrows. Median grain size is indicated by a red arrow. (c) Bar plots (gray) show estimated volume frequency for each grain size class (Section 2.4.1; Appendix B). Red curves show the cumulative volume frequency as a function of grain size. (d) The distributions of c -axis orientations in stereoplot with one point per pixel, displayed as point plots (with 5,000 randomly selected points). Contoured stereoplots are also shown, colored by multiples of a uniform distribution (MUD) with a half-width of 7.5° . (e) Green bars represent the number frequency density (Φ ; Section 2.4.2; Appendix D) of c -axes at different angles to the compression axis (θ) with an interval of 0.1° . Gold bars represent the differences of Φ for c -axes between each deformed sample and the undeformed sample at each θ interval. The gray area marks the range of θ that corresponds to high reduced Schmid factors ($S > 0.4$; Figure 1b). (f) Purple bars represent the number frequency density (Φ) of c -axes at different reduced Schmid factors (S) with an interval of 0.005. Blue bars represent the differences of Φ for c -axes between each deformed sample and the corresponding undeformed sample at each S interval.

Figure 3. Comparing the normalised values (Section 2.5) of measured mechanical data (colored black) and modeled mechanical data (colored non-black). The deformation conditions for each row are the same as in Figure 2. For the first three columns, the mechanical models are the same as those used in Figure 2. (d) Comparing the measured normalised strain rate (Equation 13; colored black) with the modeled normalised strain rate (Equation 14) using the grain-size-sensitive model (colored red) or the CPO-only model (colored purple). (h), (l), (p) Comparing the measured normalised stress drop (Equation 16) (colored black) with the modeled normalised stress drop (Equation 18) using the grain-size-sensitive model (colored red) or the CPO-only model (colored purple).

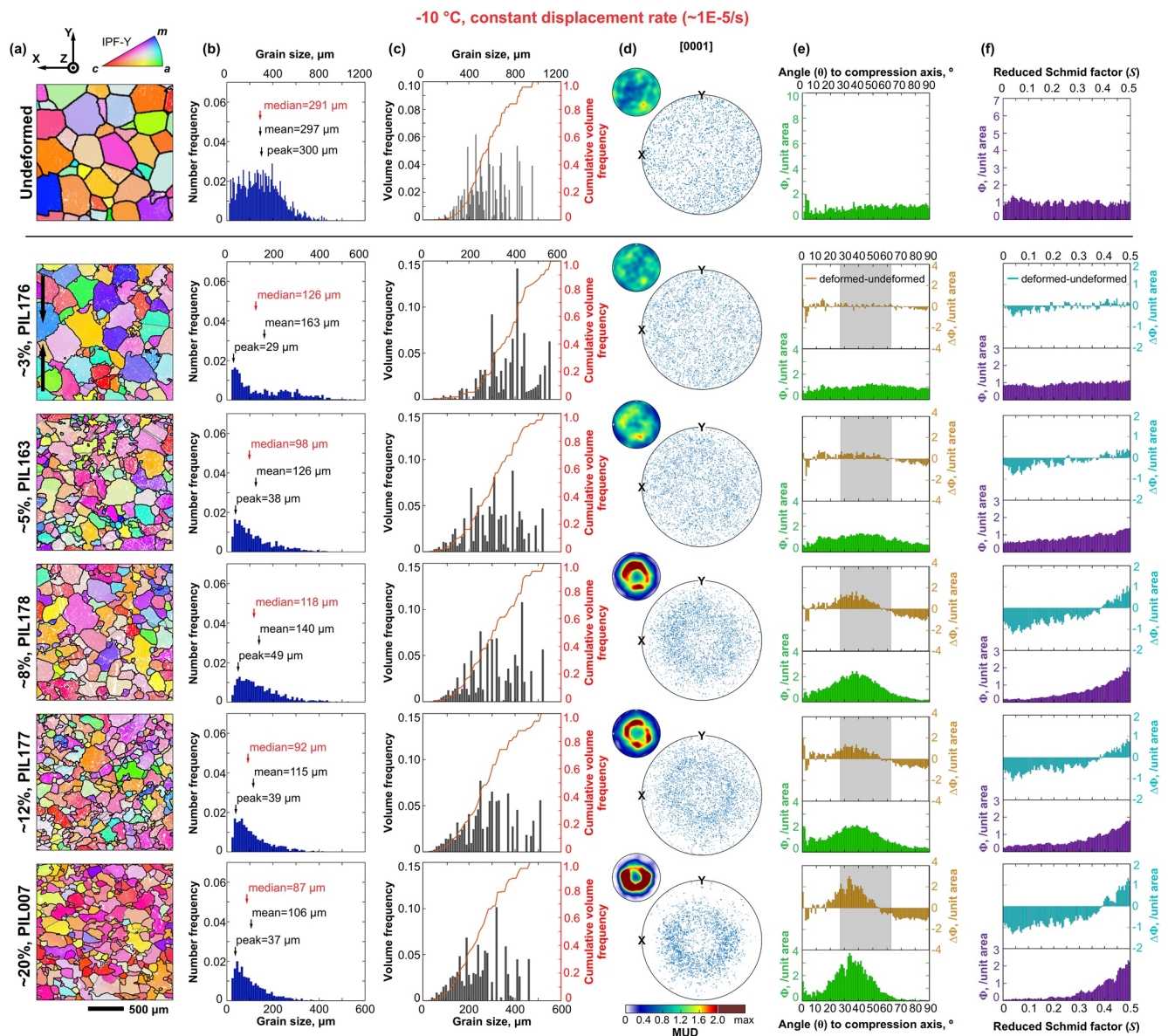


Figure 5. Microstructural analyses of deformed ice samples at -10°C under uniaxial compression with constant displacement rate ($\dot{\epsilon} \sim 1 \times 10^{-5} \text{ s}^{-1}$). The descriptions of columns (a–f) are the same as Figure 4.

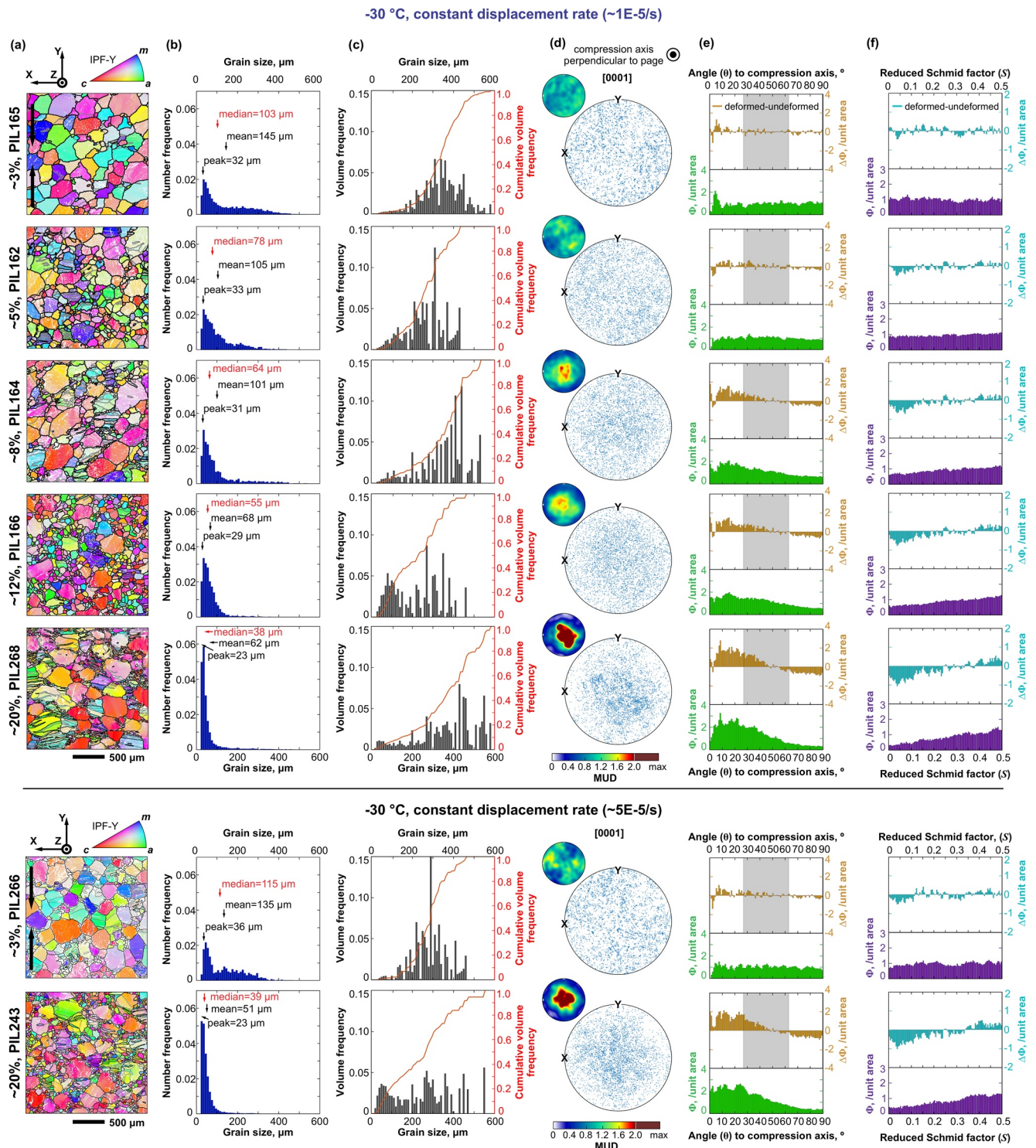
4. Discussion

4.1. Measured Mechanical Data and Deformation Mechanisms

4.1.1. Measured Mechanical Data

Under constant load, the strain rate-strain curves (colored black, Figures 2a–2c, Section 3.1.1) and the enhancement factor values of ~ 2 (ratio between the strain rate at strains of $\epsilon \geq 8\%$ and the minimum strain rate) (Table 4, Figure 3d) generally match published constant load experiments (Budd & Jacka, 1989; Jacka & Li, 2000; Wilson & Peternell, 2012).

Under constant displacement rate, the stress-strain curves (black curves, Figure 2, Section 3.1.2) show the percentage of stress-drop from peak at 20% strain ($\sim 31\text{--}38\%$) has no apparent correlations with temperature or strain rate (Tables 5 and 6, Figures 3h, 3l, and 3p). This observation matches published experiments that cover a much wider temperature and/or strain rate ranges (Section S2 of the Supporting Information S1; Durham et al., 1983, 1992; Piazzolo et al., 2013; Qi et al., 2017; Vaughan et al., 2017; Wilson et al., 2019).



4.1.2. Deformation and Recrystallization Mechanisms

The microstructures and deformation mechanisms of these samples have been discussed in detail previously (Fan et al., 2020; Fan, Prior, Cross, et al., 2021). To summarize those papers:

1. At high temperatures ($\geq -10^{\circ}\text{C}$), samples exhibit microstructures characteristic of rapid grain boundary migration, which favors the competitive growth of grains in easy slip orientations (c -axes at $\sim 45^{\circ}$ from compression), leading to the formation of cone-shaped c -axis CPOs, centered around the compression direction (Figures 4d and 5d).
2. Dynamic recovery leads to the progressive development of intragranular (subgrain) boundaries (colored gray, Figures 4a–6a).
3. With increasing strain, small recrystallized grains nucleate at the expense of large, original grains, forming a core-and-mantle structure with fine-grained networks of recrystallized grains. Recrystallized grains have much weaker CPOs than their neighboring parent grains, suggesting that grain nucleation occurs via either (1) subgrain rotation recrystallization followed by grain boundary sliding that randomizes the CPO, or (2) spontaneous nucleation of fine grains with random orientations (Fan et al., 2020).
4. As temperature decreases, lattice rotation (due to dislocation glide on the basal plane) becomes increasingly important. Basal planes progressively rotate into the compression-normal plane, producing a c -axis cluster or narrow-cone around the compression axis particularly at low temperatures, $\leq -20^{\circ}\text{C}$ (Figure 6d).
5. All the deformed samples have a major volume frequency peak corresponding to the large, original grains (Figures 4c–6c). A secondary volume frequency peak at finer sizes (corresponding to recrystallized grains) only becomes obvious at -30°C with high strains (Figure 6c). Recrystallized grains are therefore volumetrically insignificant for most of the ice samples analyzed in this study.

4.2. Contributions of Microstructural Evolution to Strain Weakening

The stresses and strain rates predicted by the mechanical models generally match the experimental measurements in magnitude (Figure 2; Section 3.3.1), indicating that they provide a certain level of reliability in the estimation of ice strength, at least under laboratory conditions. These data, as well as the normalised mechanical data, further show that strain weakening cannot be predicted by mechanical models that do not consider microstructural evolution (see first column in Figures 2 and 3). Thus, to accurately estimate ice strength and enhancement in glaciers and ice sheets, it is necessary to account for the evolving microstructural state of ice.

4.2.1. Grain Size Reduction

Under all conditions, the median grain size and grain size distribution of each sample shifts toward finer grain sizes with increasing strain, due to the nucleation of fine grains at the expense of large, original grains (Figures 4b–6b). Intuitively, we might expect samples to weaken as grain size decreases, due to the activation of GBS at fine grain sizes. However, the grain-size-sensitive models do not predict any strain weakening (red symbols, Figures 2 and 3). On the contrary, the grain-size-sensitive models actually predict a small degree of strain hardening (e.g., Figures 2, 3b, 3f, 3j, and 3n) due to the modest increase in strain rate that arises from sample shortening. Thus, these models imply that grain size has little impact on the strength of ice under the high temperature ($T_h = 0.89\text{--}0.99$), relatively high stress (>1 MPa) conditions explored in this study. We suggest that grain size plays a negligible role in strain weakening here because, even though fine grains become more abundant with increasing strain, they occupy only an insignificant fraction of each sample volume (Figures 4c–6c; Section 3.2.1). Consequently, bulk ice strength is governed by the volumetrically dominant, large, original grains, both at low and high strains.

The grain-size-sensitive model also predicts similar ice strengths when incorporated with either median grain sizes or full grain size distribution data (red symbols, Figure 2). Thus, it may generally be sufficient to model ice strength using a (simple) single value of median grain size, rather than the (more sophisticated) full grain size distribution.

It is worth noting that even though grain size reduction yields little influence over strain weakening at the experimental conditions explored here, the composite flow law (Goldsby & Kohlstedt, 1997, 2001) suggests that GBS still plays a significant role in accommodating strain. To illustrate this, we plot deformation mechanism

maps (grain size vs. stress) for each temperature explored here, with strain rate contours calculated according to Goldsby and Kohlstedt (1997, 2001) (Figure 7). On each map, symbols are plotted to represent stress-grain size data from this study, and from previous studies by other groups. All of these data summarized in Table 7. Details of the processing of published data are summarized in Appendix E. Figure 7 shows that across a broad range of temperatures, stresses, and strain rates, the experimental stresses and grain sizes all lie close to the deformation mechanism boundary (thick solid black line, Figure 7), where the contribution of dislocation creep equals to GBS-limited creep. More importantly, the grain size-stress relationship (i.e., grain size piezometer) (transparent heavy brown line) summarized by Jacka and Li (1994) using ice samples deformed to >15% strain at -10 to -0.1°C generally coincides with or lies close to the deformation mechanism boundary. These observations indicate that, the contributions of dislocation creep and GBS-limited creep to the total strain rate are roughly equal at both low and high strains. Moreover, for most of the data points, the ratio between the strain rates provided by dislocation creep and GBS-limited creep is <10 ; thus, in most of the samples examined here, GBS-limited creep accommodates at least 10% of the total deformation. Note, however, that basal dislocation glide contributes significantly to strain accommodation in the GBS-limited creep regime; thus, the proportion of deformation accommodated by GBS itself may be $<10\%$.

Figure 7 also demonstrates that for experiments performed under relatively high stresses (≥ 1 MPa), the stress-grain size data migrate from the dislocation creep regime toward the GBS-limited creep regime with increasing strain (Figures 7b–7f). At low stresses (~ 0.4 MPa; Jacka & Maccagnan, 1984), on the other hand, the data points shift from the GBS-limited creep regime toward the dislocation creep regime with increasing strain (Figure 7a). These trends probably indicate that grain size reduction dominates at high stresses, whereas grain growth dominates at low stresses.

4.2.2. CPO Development

The CPO-only model predicts strain weakening across all conditions, manifested as a strain rate enhancement under constant load conditions, and a stress drop under constant rate conditions (compare purple symbols and black curves in Figures 2 and 3), as observed in the experimental mechanical data. Moreover, at -10 and -30°C with $\sim 1 \times 10^{-5} \text{ s}^{-1}$ strain rate, the percentage of stress drop from peak stress predicted from the CPO-only model generally matches experimental measurements at each strain (Figures 3h and 3l). Thus, all of the strain weakening observed in this study can be explained by CPO development.

At high temperatures ($\geq -10^{\circ}\text{C}$), *c*-axes evolve toward a small circle (open cone) distribution around the compression axis (Figures 4d and 5d), whereas at low temperatures (-30°C), *c*-axes evolve toward a single cluster parallel with the compression axis (Figure 6d). The cone-shaped *c*-axis alignment results from grains evolving toward easy slip orientations—that is, *c*-axes inclined 30 – 60° from the compression axis (Figure 4e)—corresponding to high reduced Schmid factors of $S = 0.4$ – 0.5 (Figures 4f and 1b). Thus, cone CPO development should produce an increase in the bulk reduced Schmid factor, S_{bulk} , resulting in sample softening and strain weakening at high temperatures, per CPO-only model (Equation 8 and 9; Figure 3g). At low temperatures on the other hand, we intuitively expect CPO development to produce strain hardening, since *c*-axes progressively rotate toward hard orientations—i.e., *c*-axes inclined $<20^{\circ}$ from the compression axis (Figure 5e)—corresponding to $S \leq 0.3$ (Figure 1b). However, our data show that even at -30°C , where *c*-axes are rotating into hard slip orientations, the number of *c*-axes in high-*S* (easy slip) orientations remains significant (Figures 5e and 5f). Consequently, the bulk reduced Schmid factor, S_{bulk} , still increases with strain (Table 6), and thus leads to strain weakening in CPO-only model (Equation 8 and 9; Figures 3k and 3o). The observation of many grains with *c*-axes in high-*S* orientations at both high and low temperatures can be explained by the rate of strain-induced GBM (which favors the growth of grains in easy slip, high-*S* orientations) being similar across the range of temperatures explored here (as examined by Fan, Prior, Cross, et al., 2021). GBM rates are similar among low and high temperature conditions because GBM is controlled by both grain boundary mobility and the driving force for boundary migration (Humphreys et al., 2017)—grain boundary mobility decreases with decreasing temperature (Azuma et al., 2012), whereas the GBM driving force depends on the stress magnitude (which increases with decreasing temperature, if strain rate remains unchanged—see Figure 2; Fan, Prior, Cross, et al., 2021).

4.2.3. Strain Weakening Mechanisms Across a Broader Range of Conditions

In the models presented here, grain size evolution (reduction) does not produce strain weakening, while CPO evolution is able to account for all of the observed weakening. Thus, we suggest that CPO development is entirely

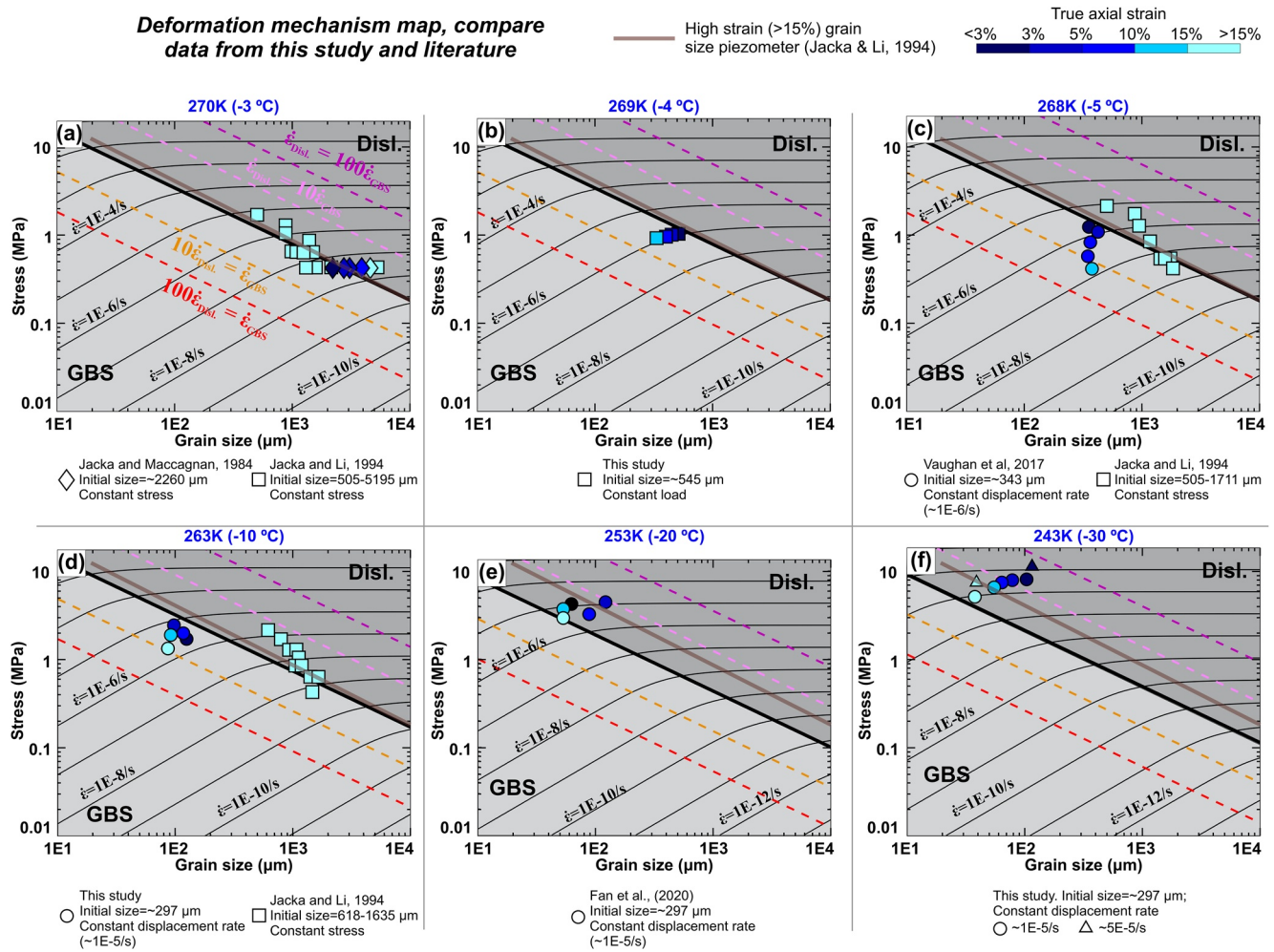


Figure 7. Deformation mechanism maps that display the relationship between the three macroscopic variables: stress (y-axis), grain size (x-axis) and strain rate (contours with thin black lines) at different temperatures. Strain rate contours are calculated using corresponding flow law parameters (Table 3, from Kuiper, Weikusat, et al., 2020, Kuiper, De Bresser, et al., 2020) for dislocation creep (Equation 4) and GBS-limited creep regime (Equation 7). Thick black solid line represents the deformation mechanism boundary, at where dislocation creep strain rate equals to GBS strain rate. Dashed colored lines represent the ratio between the dislocation creep strain rate and the GBS strain rate. Points representing stress-grain size relationships using experimental data from this study and published literature (Fan et al., 2020; Jacka & Li, 1994; Jacka & Maccagnan, 1984; Vaughan et al., 2017) are superposed over deformation mechanism maps at different temperatures. Transparent brown line represents the grain size-stress relationship summarized by Jacka and Li (1994) at relatively high strains (> ~15%).

responsible for strain weakening across the range of conditions explored here ($T = -4$ to -30°C ; strain rate $\approx 10^{-5}$ s^{-1} ; stress ≈ 1 – 10 MPa). To quantify the relative contributions of CPO and grain size to strain weakening across a wider range of strain rate/stress, we compare this study with published ice uniaxial compression experiments that provide mechanical data as well as CPO and/or grain size data (Jacka & Maccagnan, 1984; Qi et al., 2017; Vaughan et al., 2017). The EBSD data from Vaughan et al. (2017) and Qi et al. (2017) were re-processed following the same procedure used in this study (Sections 2.2, 2.4) to acquire median grain size and bulk reduced Schmid factor, S_{bulk} measurements. Jacka and Maccagnan (1984) provide mean grain size and c -axis point orientation data—the c -axis point data were digitized using an automated algorithm in MATLAB, from which S_{bulk} measurements were calculated. For Jacka and Maccagnan (1984) and Vaughan et al. (2017), which include experiments performed to various shortening strains, the modeled strain rates or stresses were normalised relative to their values at the minimum strain rate or peak stress, respectively (as described above in Section 2.5). Qi et al. (2017), who deformed ice samples under different strain rates, only provide microstructural data at $\sim 20\%$ strain. Based on our experiments, the grain size at peak stress is hard to predict due to grain size reduction even at low strains (Figures 4b–6b). However, the CPO is generally still close to random at the peak stress (Figures 4d–6d). Therefore, for the data from Qi et al. (2017), we applied only Azuma's flow law to model the

Table 7
Summary of Strain Rate, Stress, and Grain Size of Data From This Study and the Literature

Study	Sample no.	T (°C)	True axial strain ^a	Initial grain size (μm) ^b	Measured strain rate (s ⁻¹) ^c	Converted strain rate (s ⁻¹) ^d	Strain rate estimated from deformation mechanism maps	Measured grain size, d-μm; A-mm ^{2c}	Converted grain size (μm)	Measured stress at the end of experiment (MPa) ^f	Converted stress (MPa) ^g
This study	OIL009	-4	0.01	297	$\dot{\epsilon} = 1.11\text{E}-06$	1.11E-06	1.10E-06	$d = 501$	501	$\sigma = 1.02$	1.02
	OIL008		0.04		Not recorded		1.20E-06	$d = 453$	453	$\sigma = 0.99$	0.99
	OIL007		0.08		$\dot{\epsilon} = 1.78\text{E}-06$	1.78E-06	1.30E-06	$d = 411$	411	$\sigma = 0.95$	0.95
	OIL006		0.13		$\dot{\epsilon} = 1.22\text{E}-06$	1.22E-06	1.60E-06	$d = 337$	337	$\sigma = 0.9$	0.90
	PIL176	-10	0.03		$\dot{\epsilon} = 1.04\text{E}-05$	1.04E-05	2.21E-06	$d = 126$	126	$\sigma = 1.7$	1.70
	PIL163		0.05		$\dot{\epsilon} = 1.06\text{E}-05$	1.06E-05	6.73E-06	$d = 98$	98	$\sigma = 2.42$	2.42
	PIL178		0.08		$\dot{\epsilon} = 1.19\text{E}-05$	1.19E-05	3.37E-06	$d = 118$	118	$\sigma = 1.97$	1.97
	PIL177		0.12		$\dot{\epsilon} = 1.21\text{E}-05$	1.21E-05	4.00E-06	$d = 92$	92	$\sigma = 1.9$	1.90
	PIL007		0.19		$\dot{\epsilon} = 1.22\text{E}-05$	1.22E-05	1.99E-06	$d = 87$	87	$\sigma = 1.33$	1.33
	PIL165	-30	0.03		$\dot{\epsilon} = 1.09\text{E}-05$	1.09E-05	4.04E-05	$d = 103$	103	$\sigma = 8.15$	8.15
	PIL162		0.05		$\dot{\epsilon} = 1.10\text{E}-05$	1.10E-05	3.61E-05	$d = 78$	78	$\sigma = 7.87$	7.87
	PIL164		0.07		$\dot{\epsilon} = 1.07\text{E}-05$	1.07E-05	2.80E-05	$d = 64$	64	$\sigma = 7.31$	7.31
	PIL166		0.12		$\dot{\epsilon} = 1.20\text{E}-05$	1.20E-05	1.81E-05	$d = 55$	55	$\sigma = 6.45$	6.45
	PIL268		0.21		$\dot{\epsilon} = 1.31\text{E}-05$	1.31E-05	8.65E-06	$d = 38$	38	$\sigma = 5$	5.00
	PIL266		0.03		$\dot{\epsilon} = 5.40\text{E}-05$	5.40E-05	1.43E-04	$d = 115$	115	$\sigma = 11.26$	11.26
	PIL243		0.24		$\dot{\epsilon} = 6.70\text{E}-05$	6.70E-05	3.16E-05	$d = 39$	39	$\sigma = 7.35$	7.35
	Jacka and Maccagnan (1984)	A1	-3	0.01	2,260	$\dot{\gamma}_{oc} = 2.00\text{E}-08$	2.84E-08	6.33E-08	$d = 2,200$	2,200	$\tau_{oc} = 0.2$
A2			0.03		$\dot{\gamma}_{oc} = 3.60\text{E}-08$	5.17E-08	5.15E-08	$d = 2,800$	2,800	$\tau_{oc} = 0.2$	0.42
A3			0.04		$\dot{\gamma}_{oc} = 4.00\text{E}-08$	5.77E-08	4.77E-08	$d = 3,100$	3,100	$\tau_{oc} = 0.2$	0.42
A4			0.10		$\dot{\gamma}_{oc} = 6.10\text{E}-08$	9.04E-08	4.07E-08	$d = 3,900$	3,900	$\tau_{oc} = 0.2$	0.42
A5			0.11		$\dot{\gamma}_{oc} = 6.30\text{E}-08$	9.37E-08	3.69E-08	$d = 4,600$	4,600	$\tau_{oc} = 0.2$	0.42
A6			0.22		$\dot{\gamma}_{oc} = 6.10\text{E}-08$	9.53E-08	3.69E-08	$d = 4,600$	4,600	$\tau_{oc} = 0.2$	0.42
A7			0.51		$\dot{\gamma}_{oc} = 6.00\text{E}-08$	1.02E-07	3.69E-08	$d = 4,600$	4,600	$\tau_{oc} = 0.2$	0.42
Jacka and Li (1994)	N/A	-3	>0.15	1,240	$\dot{\gamma}_{oc} = 1.10\text{E}-07$	N/A	8.65E-08	$A = 2$	1,596	$\tau_{oc} = 0.2$	0.42
				1,240	$\dot{\gamma}_{oc} = 2.20\text{E}-07$		2.56E-07	$A = 1.8$	1,514	$\tau_{oc} = 0.3$	0.64
				1,240	$\dot{\gamma}_{oc} = 6.40\text{E}-07$		6.30E-07	$A = 1.5$	1,382	$\tau_{oc} = 0.4$	0.85
				1,240	$\dot{\gamma}_{oc} = 1.10\text{E}-06$		1.65E-06	$A = 0.6$	874	$\tau_{oc} = 0.5$	1.06
				1,240	$\dot{\gamma}_{oc} = 2.60\text{E}-06$		2.88E-06	$A = 0.6$	874	$\tau_{oc} = 0.6$	1.27
				1,240	$\dot{\gamma}_{oc} = 8.80\text{E}-06$		9.61E-06	$A = 0.2$	505	$\tau_{oc} = 0.8$	1.70
				2,300	$\dot{\gamma}_{oc} = 6.00\text{E}-08$		3.46E-08	$A = 21.2$	5,195	$\tau_{oc} = 0.2$	0.42
				2,500	$\dot{\gamma}_{oc} = 1.32\text{E}-07$		2.84E-07	$A = 1.4$	1,335	$\tau_{oc} = 0.3$	0.64
				2,900	$\dot{\gamma}_{oc} = 1.12\text{E}-07$		3.29E-07	$A = 1$	1,128	$\tau_{oc} = 0.3$	0.64
				2,900	$\dot{\gamma}_{oc} = 9.50\text{E}-08$		3.66E-07	$A = 0.8$	1,009	$\tau_{oc} = 0.3$	0.64
				1,700	$\dot{\gamma}_{oc} = 3.25\text{E}-08$		1.05E-07	$A = 1.4$	1,335	$\tau_{oc} = 0.2$	0.42
				798	$\dot{\gamma}_{oc} = 2.43\text{E}-07$		2.46E-07	$A = 2$	1,596	$\tau_{oc} = 0.3$	0.64
				798	$\dot{\gamma}_{oc} = 2.54\text{E}-07$		2.84E-07	$A = 1.4$	1,335	$\tau_{oc} = 0.3$	0.64
				798	$\dot{\gamma}_{oc} = 3.63\text{E}-07$		6.49E-08	$A = 3.6$	2,141	$\tau_{oc} = 0.2$	0.42
		-5		1,240	$\dot{\gamma}_{oc} = 6.00\text{E}-08$		3.60E-08	$A = 2.7$	1,854	$\tau_{oc} = 0.2$	0.42
				1,240	$\dot{\gamma}_{oc} = 3.30\text{E}-07$		3.61E-07	$A = 1.1$	1,184	$\tau_{oc} = 0.4$	0.85
			1,240	$\dot{\gamma}_{oc} = 1.40\text{E}-06$		1.50E-06	$A = 0.7$	944	$\tau_{oc} = 0.6$	1.27	

Table 7
Continued

Study	Sample no.	T (°C)	True axial strain ^a	Initial grain size (μm) ^b	Measured strain rate (s ⁻¹) ^c	Converted strain rate (s ⁻¹) ^d	Strain rate estimated from deformation mechanism maps	Measured grain size, d-μm; A-mm ^{2c}	Converted grain size (μm)	Measured stress at the end of experiment (MPa) ^f	Converted stress (MPa) ^g
				1,240	$\dot{\gamma}_{oc} = 5.60E-06$		4.20E-06	A = 0.6	874	$\tau_{oc} = 0.8$	1.70
				1,240	$\dot{\gamma}_{oc} = 1.30E-05$		1.09E-05	A = 0.2	505	$\tau_{oc} = 1$	2.12
				1,600	$\dot{\gamma}_{oc} = 6.67E-08$		7.94E-08	A = 1.7	1,471	$\tau_{oc} = 0.25$	0.53
				1,600	$\dot{\gamma}_{oc} = 6.42E-08$		7.04E-08	A = 2.3	1,711	$\tau_{oc} = 0.25$	0.53
				1,600	$\dot{\gamma}_{oc} = 6.79E-08$		7.43E-08	A = 2	1,560	$\tau_{oc} = 0.25$	0.53
		-10		1,240	$\dot{\gamma}_{oc} = 7.00E-09$		6.52E-09	A = 1.7	1,471	$\tau_{oc} = 0.2$	0.42
				1,240	$\dot{\gamma}_{oc} = 4.80E-08$		1.88E-08	A = 2.1	1,635	$\tau_{oc} = 0.3$	0.64
				1,240	$\dot{\gamma}_{oc} = 9.80E-08$		5.54E-08	A = 1.1	1,184	$\tau_{oc} = 0.4$	0.85
				1,240	$\dot{\gamma}_{oc} = 2.00E-07$		1.18E-07	A = 1	1,128	$\tau_{oc} = 0.5$	1.06
				1,240	$\dot{\gamma}_{oc} = 3.80E-07$		2.26E-07	A = 0.9	1,071	$\tau_{oc} = 0.6$	1.27
				2,718	$\dot{\gamma}_{oc} = 2.90E-08$		2.04E-08	A = 1.6	1,427	$\tau_{oc} = 0.3$	0.64
				2,718	$\dot{\gamma}_{oc} = 7.20E-08$		5.85E-08	A = 0.9	1,071	$\tau_{oc} = 0.4$	0.85
				2,718	$\dot{\gamma}_{oc} = 3.50E-08$		2.35E-07	A = 0.7	944	$\tau_{oc} = 0.6$	1.27
				2,718	$\dot{\gamma}_{oc} = 1.10E-08$		6.83E-07	A = 0.5	798	$\tau_{oc} = 0.8$	1.70
				2,718	$\dot{\gamma}_{oc} = 3.60E-08$		1.63E-06	A = 0.3	618	$\tau_{oc} = 1$	2.12
Vaughan et al. (2017)	def014	-5	0.01	343	$\dot{\epsilon} = 1.00E-06$	1.01E-06	2.50E-06	d = 355	355	$\sigma = 1.12$	1.12
	def013		0.03			1.03E-06	1.52E-06	d = 425	425	$\sigma = 1.13$	1.13
	def012		0.05			1.05E-06	9.11E-07	d = 364	364	$\sigma = 1.22$	1.22
	def011		0.08			1.08E-06	4.43E-07	d = 349	349	$\sigma = 1.17$	1.17
	def010		0.11			1.11E-06	2.10E-07	d = 377	377	$\sigma = 1.2$	1.2
Fan et al. (2020)	PIL254	-20	0.03	297	$\dot{\epsilon} = 1.06E-05$	1.06E-05	1.31E-05	d = 62	62	$\sigma = 4.25$	4.25
	PIL182		0.04		$\dot{\epsilon} = 8.94E-06$	8.94E-06	1.32E-05	d = 122	122	$\sigma = 4.44$	4.44
	PIL184		0.08		$\dot{\epsilon} = 1.17E-05$	1.17E-05	4.53E-06	d = 89	89	$\sigma = 3.24$	3.24
	PIL185		0.12		$\dot{\epsilon} = 1.19E-05$	1.19E-05	8.61E-06	d = 53	53	$\sigma = 3.68$	3.68
	PIL255		0.20		$\dot{\epsilon} = 1.28E-05$	1.28E-05	4.25E-06	d = 53	53	$\sigma = 2.93$	2.93

^aStrain at the end of uniaxial compression experiment is converted to true axial strain following methods described by Fan et al. (2020). ^bInitial grain size is median grain size for data from this study, Vaughan et al. (2017) and Fan et al. (2020). Initial grain size is taken directly from Jacka and Maccagnan (1984), and it is calculated using mean linear intercept method (Appendix E). Initial grain size is converted from averaged grain area by Eq. (E.2) for data from Jacka and Li (1994). ^c $\dot{\epsilon}$ is true axial strain rate. $\dot{\gamma}_{oc}$ is octahedral shear strain rate. $\dot{\epsilon}$ is engineering strain rate. ^d $\dot{\gamma}_{oc}$ and $\dot{\epsilon}$ are converted to $\dot{\epsilon}$ using methods described by Fan et al. (2020). ^eMeasured grain size is median grain size for data from this study, Vaughan et al. (2017) and Fan et al. (2020). Measured grain size is taken directly from Jacka and Maccagnan (1984), and it is calculated using mean linear intercept method (Appendix E). Measured grain size is converted from averaged grain area by Eq. (E.2) for data from Jacka and Li (1994). ^f σ is differential axial stress. τ_{oc} is octahedral shear stress. ^g τ_{oc} is converted to σ using methods described by Fan et al. (2020).

mechanical effects of CPO development. The modeled stress at each finite strain was normalised relative to the peak stress estimated for a random CPO ($S_{bulk} = 0.25$).

For constant load/stress experiments (-4°C series in this study; data from Jacka & Maccagnan, 1984), we calculate the ratio between the normalised measured strain rate, $\bar{\epsilon}_{measure}$ (Equation 13) and the normalised modeled strain rate, $\bar{\epsilon}_{model}$ (Equation 14) at each finite strain (Figure 8a). For experiments with constant displacement rate ($-10, -30^\circ\text{C}$ series in this study; data from Qi et al., 2017 and Vaughan et al., 2017), we calculate the ratio between the normalised measured stress drop, $\Delta\bar{\sigma}_{measure}$ (Equation 16) and the normalised modeled stress drop, $\Delta\bar{\sigma}_{model}$ (Equation 18) (Figure 8b). Full details of these data are provided in Section S3 in supporting Information S1. Figure 8 shows that the measured strain rate enhancement (for constant load/stress experiments) and stress drops (for constant displacement rate experiments) are generally close to the modeled results using

CPO-only model, that is, $\bar{\epsilon}_{\text{measure}}/(\bar{\epsilon}_{\text{model}}(\text{CPO} - \text{only})) \approx 1$; $\Delta\bar{\sigma}_{\text{measure}}/(\Delta\bar{\sigma}_{\text{model}}(\text{CPO} - \text{only})) \approx 1$ (purple symbols, Figure 8). On the other hand, the grain-size-sensitive model generally underestimates the measured strain weakening, that is, $\bar{\epsilon}_{\text{measure}}/(\bar{\epsilon}_{\text{model}}(\text{GSS})) > 2$; $\Delta\bar{\sigma}_{\text{measure}}/(\Delta\bar{\sigma}_{\text{model}}(\text{GSS})) \gg 5$ (red symbols, Figure 8). In some cases, the grain-size-sensitive model even predicts strain hardening, that is, $\Delta\bar{\sigma}_{\text{measure}}/(\Delta\bar{\sigma}_{\text{model}}(\text{GSS})) < 0$ (red symbols, Figure 8b), which is at odds with the experimental observations of strain weakening. Thus, even across a broader range of strain rates than those explored in our experiments, CPO development remains the dominant contributor to strain weakening. Weakening due to grain size reduction remains negligible.

4.3. Implications for Natural Ice Flow

Even though all the mechanical models predict ice strengths that generally match the magnitudes of measured ice strength, only Azuma's CPO-only flow law matches the observed patterns of strain weakening (Figures 2 and 3). This observation suggests that strain weakening in ice can be estimated on the basis of *c*-axis orientations alone, without regard for grain size evolution, at least under the relatively high stress, high temperature conditions explored here. Therefore, acquiring ice sheet scale measurements of *c*-axis orientation would be valuable for better constraining terrestrial ice flow mechanics and rates of ice mass discharge. Terrestrial ice *c*-axis data are usually provided by microstructural analyses of ice cores (e.g., Azuma et al., 1999; Weikusat et al., 2017). However, recent developments in cryo-seismology may provide a cost-effective way of estimating ice *c*-axis orientations across a wide region (on the order of several square kilometres or more) via inversion of seismic anisotropy data (Lutz et al., 2020; Smith et al., 2017).

It is known that under natural conditions, two important facts including impurities and water content, which are not explored in this study, might also influence the physical properties of natural ice masses and lead to strain weakening:

1. Impurities including insoluble particles (e.g., dust), solutes (e.g., salts), and air bubbles (Eichler et al., 2017; Hammonds & Baker, 2018; Obbard & Baker, 2007; Steinbach et al., 2016). The accumulation of microparticles or air bubbles along grain boundaries can reduce grain boundary mobility, inhibiting normal grain growth, enhancing strain localization, and thereby promoting further grain size reduction (Herwegh et al., 2011; Steinbach et al., 2016). Meanwhile, soluble impurities, such as HF and HCl, can enhance mechanical softening in ice, because F⁻ or Cl⁻ ions are easy to substitute at locations of O atoms in ice-Ih lattices, creating additional point defects that enhance dislocation creep (Fujita et al., 2014; Jones, 1967; Jones & Glen, 1969).
2. Meltwater is an important component of natural ice, and it can be produced via surface melting and/or shear heating within ice shear margins (Cuffey & Paterson, 2010). Laboratory experiments show the presence of water could attenuate the internal stress, facilitate grain boundary migration and/or nucleation, and reduce ice viscosity (De La Chapelle et al., 1999; Duval, 1977; Haseloff et al., 2019). Consequently, meltwater content might also promote strain weakening and causing strain localization within terrestrial ice shear margins (Hunter et al., 2021).

4.4. Implications for Rock-Forming Minerals and Lithospheric Deformation

Strain weakening also enables deformation to localize into lithospheric shear zones and plate boundaries (e.g., Little et al., 2015; Skemer et al., 2009; White et al., 1980), and therefore plays a central role in plate tectonics. In order to accurately model plate-scale lithospheric deformation, we therefore need a comprehensive understanding of the microphysical processes that produce strain weakening across a broad range of conditions in rock-forming minerals. Many studies have linked strain weakening at relatively low homologous temperatures ($T_h < 0.7$) to mechanisms such as grain size evolution (Karato et al., 1986; Rutter, 1995), CPO development (Schmid et al., 1987; Urai et al., 1986), partial melting (Burlini & Bruhn, 2005; Hirth & Kohlstedt, 1995), metamorphic reactions and transformations (Gordon, 1971; Poirier, 1982), water weakening (Griggs & Blacic, 1965; Karato et al., 1986; Kronenberg & Tullis, 1984) and mineral phase mixing and/or layering (Bons & Cox, 1994; Cross et al., 2020). However, we lack a comprehensive understanding of the processes that produce strain weakening in rocks and minerals at very high temperatures ($T_h > 0.7$). This is because most rock deformation rigs are limited to temperatures <1500 K, whereas many rock-forming minerals have much higher melting temperatures (e.g., ~1950 K for quartz, ~2200 K for olivine). Thus, studies of ice deformation—such as this one—provide useful

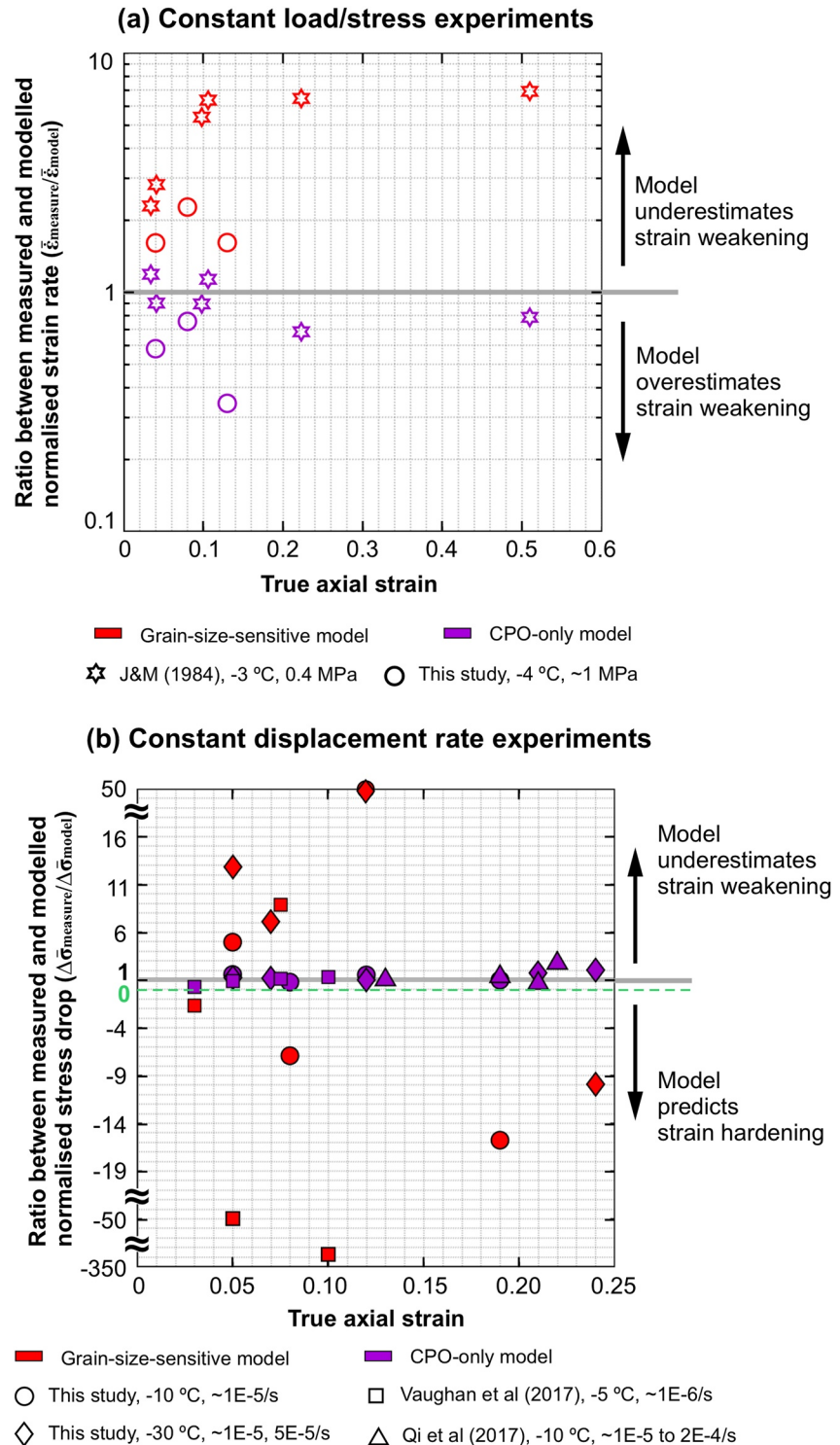


Figure 8. Modeling the relative contribution of CPO development and grain size change to the strain weakening using data from this study and published literature (Jacka & Maccagnan, 1984; Qi et al., 2017; Vaughan et al., 2017). Results using the grain-size-sensitive model (Section 2.3.2), which considers the grain size effects, are colored red; results using the CPO-only model (Section 2.3.3), which considers the CPO development, are colored purple. (a) For constant load experiments, at each finite strain, the ratio between measured normalised strain rate, $\dot{\epsilon}_{\text{measure}}$ (Equation 13), and modeled normalised strain rate, $\dot{\epsilon}_{\text{model}}$ (Equation 14), was calculated (Section 4.2.3). (b) For constant displacement rate experiments, at each finite strain, the ratio between measured normalised stress drop, $\Delta\bar{\sigma}_{\text{measure}}$ (Equation 16), and modeled normalised stress drop, $\Delta\bar{\sigma}_{\text{model}}$ (Equation 14), was calculated (Section 4.2.3).

insights into the high homologous temperature deformation of rock-forming minerals; particularly those with strong viscous anisotropy, like quartz and olivine.

Our experimental data suggest that at $T_h \geq 0.9$, strain weakening is dominated by CPO development, whereas grain size reduction plays a negligible role. In contrast, at $T_h \approx 0.7$, it has been found that strain weakening in olivine is dominated by grain size reduction, with only $\sim 30\%$ of strain weakening arising from CPO development (Hansen et al., 2012). Together, these data indicate that strain weakening can result from both grain size reduction and CPO development; however, the relative contributions of these two processes may vary systematically across different thermomechanical conditions. Grain size reduction may dominate strain weakening at low temperatures (Hansen et al., 2012), whereas CPO development may govern strain weakening at high temperatures (this study), at least for viscously anisotropic minerals—like ice, olivine, and quartz—which are very sensitive to CPO development.

5. Conclusions

1. At temperatures of -4 to -30°C ($T_h = 0.89$ – 0.99), initially isotropic, polycrystalline ice undergoes strain weakening beyond strains of 1% – 3% . Grain size reduction and CPO development coincide with strain weakening.
2. Grain sizes decrease modestly with increasing strain, particularly at lower temperatures where fine recrystallized grains progressively nucleate. To explore the role of grain size evolution in strain weakening, stress and grain size measurements were inserted into a composite ice flow law (Goldsby & Kohlstedt, 1997, 2001) that includes grain size sensitivity but does not account CPO development. The composite law suggests that both grain boundary sliding and dislocation creep contribute to sample straining under our experimental conditions. Moreover, the contribution of grain boundary sliding (to overall straining) is estimated to increase with increasing strain, due to modest bulk grain size reduction. Despite this, the composite flow law predicts a near-constant sample strength with increasing strain, in contradiction to the observed strain weakening. This result suggests that grain size reduction has comparatively little effect on strain weakening under our high homologous temperature experimental conditions.
3. In addition to grain size evolution, crystallographic preferred orientation (CPO) development is also observed with increasing strain. At lower temperatures, c -axes form a single cluster, centered around the compression axis, which should produce more hard slip with increasing strain. At higher temperatures, c -axes instead evolve toward easy slip orientations, forming an open cone (small circle) around the compression axis. To examine ice strength evolution due to CPO development, c -axis orientation statistics were incorporated into a flow law that solely considers the effect of CPO on bulk ice strength (Azuma, 1994, 1995). The CPO-only model is able to closely replicate the observed strain weakening, suggesting that CPO development is responsible for strain weakening in our experimental samples.
4. Previous studies have found that grain size reduction plays a dominant role in strain weakening at lower homologous temperatures (Hansen et al., 2012). Our data suggest that CPO development is the more effective strain weakening mechanism at higher homologous temperatures, particularly for materials with strong viscous anisotropy like ice and, we suggest, possibly olivine and quartz. Grain size reduction and associated weakening, on the other hand, may be more pronounced under high stress, low temperature conditions, where recrystallized grains are finer. Together, we suggest that strain weakening may result from both grain size reduction and CPO development, the relative contributions of which may vary as a function of temperature, grain size, stress, and strain rate.

Appendix A: Estimate the Impact of Elastic Deformation on Plastic Strain Measurement for Constant Load Experiments

For a deformed material, the measured strain using the initial and final sample dimension (e.g., Equation 1) comprises both elastic strain and plastic strain (Hill et al., 1947). The elastic strain, $\epsilon_{elastic}$, is the strain that is fully recoverable after the removal of load, and it is the ratio between the applied differential stress, σ , and the Young's modulus, E :

$$\epsilon_{elastic} = \frac{\sigma}{E} \quad (\text{A1})$$

During the deformation of metal and rocks, where the applied stress is usually very high, the elastic strain should be considered in order to deduce the correct plastic strain (Hansen et al., 2012; Hill et al., 1947).

Under the setting of constant load experiments reported in this study, the assembly of walnut wood piston (Young's modulus, E_{wood} , of ~ 11 GPa at $\sim 10\%$ moisture content, Bachtiar et al., 2017) and ice (Young's modulus, E_{ice} , ~ 9.3 GPa, Gammon et al., 1983) was subject to an initial uniaxial stress of ~ 1 MPa (Sect. 2.1.2). Therefore, based on Equation A1, the elastic strain of walnut wood and ice is 9.1×10^{-5} and 1.0×10^{-4} , respectively, both of which are at least two orders of magnitudes lower than the lowest strain of 0.01 achieved in the experiments. Therefore, we suggest the elastic strain of walnut wood piston and ice sample is generally insignificant, and they are negligible compared with the plastic strain of ice sample.

Appendix B: Estimate the Volume Fraction of Different Grain Size Classes

We estimate volume fraction for different grain size classes using the Scheil-Schwartz-Saltikov method (shortened as Saltikov method, sometimes spelled as "Saltykov method": Saltikov, 1967; Scheil, 1931; Schwartz, 1934) by assuming the grains are spherical. Numerical modeling work from Sahagian & Proussevitch (1998) shows that statistically, grain shape in 3-D has little effect on the grain size distributions captured by 2-D cross-sections. The Python-based GrainSizeTools toolbox (Lopez-Sanchez & Llana-Fúnez, 2016) was applied to estimate 3-D grain volume fraction from the data of grain number frequency as a function of grain size. The Saltikov method has been proven accurate in estimating the volume percentage with $\pm 5\%$ uncertainty for given grain size classes that correspond to the grain size class bin width of 8–16 μm (Lopez-Sanchez & Llana-Fúnez, 2016). In this study, we choose grain size class width of 10 μm as a compromise of minimizing the error of individual bins in the distribution (i.e., having enough data in each class width) and grain size sensitivity in the model (i.e., having enough number of grain size classes).

Appendix C: Deformation Boundary Condition Models

Grain size distribution has been used in grain size sensitive flow laws to quantify the control of grain size on the mechanical behavior of deformed rock and ice (Freeman & Ferguson, 1986; Kuiper, De Bresser, et al., 2020; Kuiper, Weikusat, et al., 2020; Rutter & Brodie, 1988; Ter Heege et al., 2004). The incorporation of grain size distributions into the flow laws is based on the recognition that large and small grains may behave differently during the deformation, since the strain rates related to grain size sensitive (GSS) mechanisms, such as GBS and diffusion creep, will be faster in small grains (Ghosh & Raj, 1981; Goldsby & Kohlstedt, 1997; Raj & Ghosh, 1981). Freeman and Ferguson (1986) and Ter Heege et al. (2004) applied the following two bounding end-member deformation boundary condition models.

1. Homogeneous stress model, with local strain rate varying from grain to grain.
2. Homogeneous strain rate model, with local stress varying from grain to grain.

We consider an ice sample comprising i classes of grain sizes of $d_A, d_B, d_C, \dots, d_i$ occupying volume fractions of $v_A, v_B, v_C, \dots, v_i$, respectively. For the homogeneous stress model (Figure C1a), we assume the stress for each grain size class equal to the bulk stress:

$$\sigma_{total} = \sigma_A = \sigma_B = \sigma_C = \dots = \sigma_i. \quad (C1)$$

Grain size classes have corresponding strain rates of $\dot{\epsilon}_A, \dot{\epsilon}_B, \dot{\epsilon}_C, \dots, \dot{\epsilon}_i$ (Figure C1a). The strain rate, $\dot{\epsilon}_i$, in grain size class i is calculated using the grain-size-sensitive model (Equation 6). The modeled bulk strain rate, that is, sum of volume weighted strain rates in all grain size classes, can be expressed as (Figure C1a):

$$\dot{\epsilon}_{total} = v_A \dot{\epsilon}_A + v_B \dot{\epsilon}_B + v_C \dot{\epsilon}_C + \dots + v_i \dot{\epsilon}_i. \quad (C2)$$

For homogeneous strain rate model (Figure C1b), we assume the strain rate for each grain size class equals to the bulk strain rate:

$$\dot{\epsilon}_{total} = \dot{\epsilon}_A = \dot{\epsilon}_B = \dot{\epsilon}_C = \dots = \dot{\epsilon}_i. \quad (C3)$$

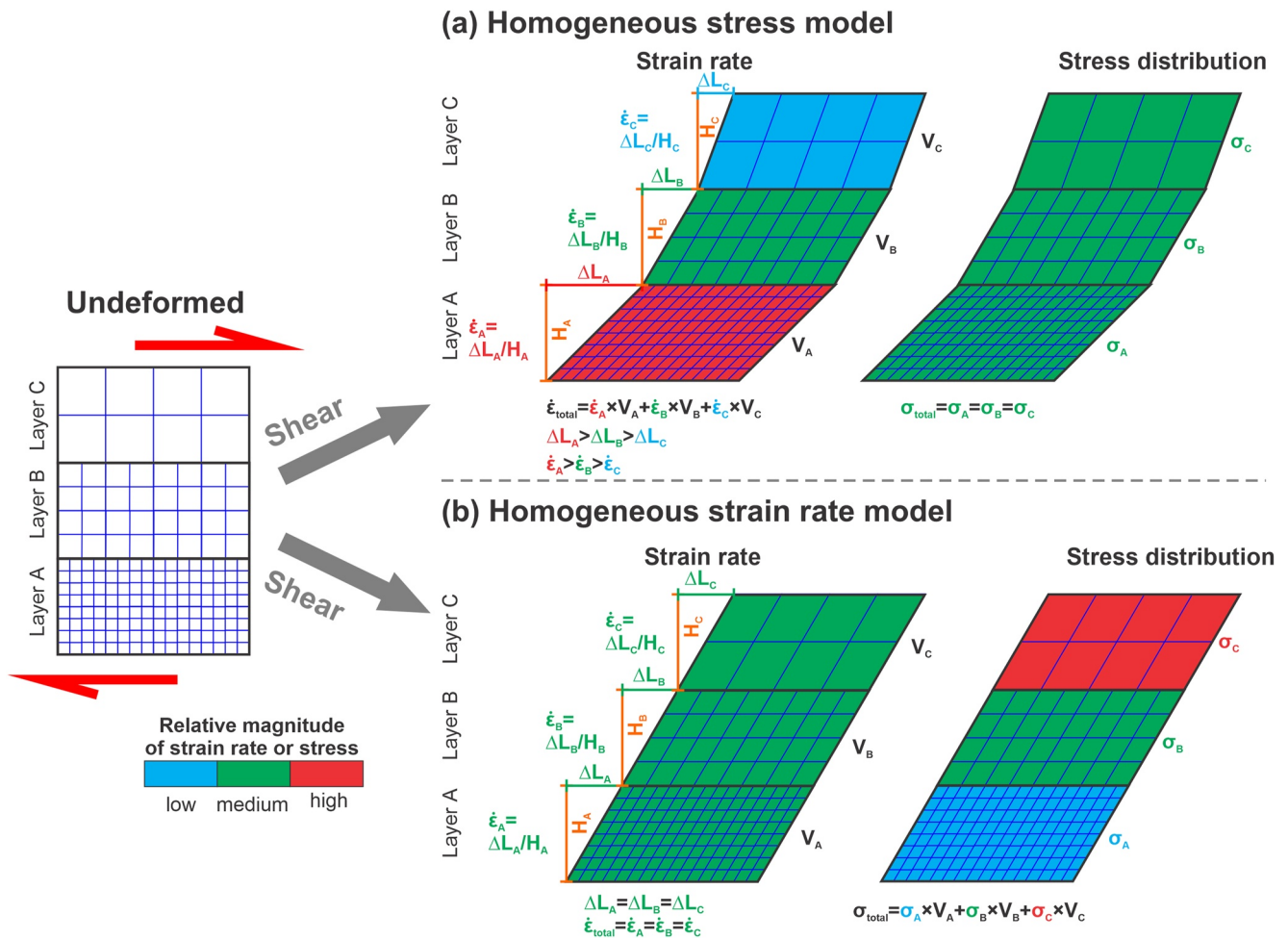


Figure C1. Schematic drawing that illustrates principles of the two end-member deformation boundary condition models (Section 2.4.1; Appendix C) of (a) homogeneous stress with local strain rate varying from grain to grain, and (b) homogeneous strain rate with local stress varying from grain to grain. Note that, for the sake of simplicity and clarity of demonstration, each grain is presented with a quadrangle, and grains with the same sizes are grouped. Undeformed sample is composed by three layers of grains; each layer contains grains with the same sizes; grain size decreases from layer C to layer A. After deformation, each grain is colored by the relative magnitude of strain rate or stress based on homogeneous stress model (a) and homogeneous strain rate model (b). For each layer, the corresponding strain rate, volume frequency and stress are marked next to it.

The stress σ_i for grain size class i corresponding to the grain-size-sensitive model can be calculated by solving Equation 6 via iteration. The modeled bulk stress, that is, sum of volume weighted stresses in all grain size classes can be expressed as (Figure C1b):

$$\sigma_{total} = U_A \sigma_A + U_B \sigma_B + U_C \sigma_C + \dots + U_i \sigma_i. \quad (C4)$$

Appendix D: Calculate the Density of c -Axes Between Given Co-Latitude Intervals

Figure D1 is a 3-D illustration of an interval between two co-latitudes of θ_1 and θ_2 that contain a certain number frequency, f , of c -axes measurements. Therefore, number frequency density (Φ), that is, number frequency per unit area, can be calculated from the ratio between number frequency, f , and the area of the co-latitude interval in 3-D, A :

$$\Phi = \frac{f}{A} \quad (D1)$$

The area of the co-latitude interval in 3-D, A , is the difference between the area of two spherical caps with the height of h_1 and h_2 (Figure D1):

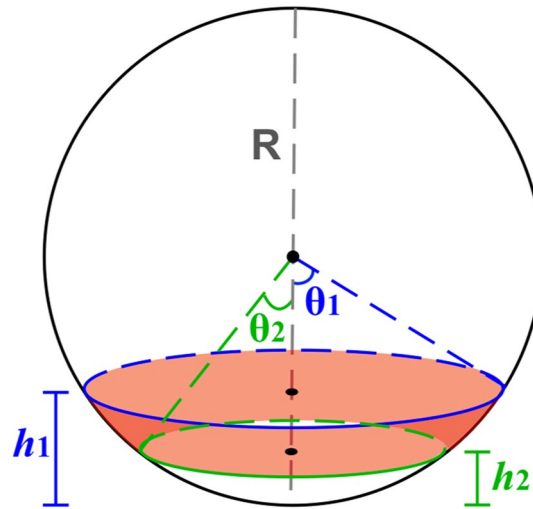


Figure D1. A 3-D illustration of an interval between two co-latitudes of θ_1 and θ_2 that contain a certain number frequency of c -axes measurements.

$$A = A_{cap1} - A_{cap2} = 2\pi R(h_1 - h_2) \quad (D2)$$

Figure D1 shows h_1 and h_2 are function of co-latitudes of θ_1 and θ_2 , respectively:

$$h_1 = R(1 - \cos\theta_1) \quad (D3)$$

$$h_2 = R(1 - \cos\theta_2)$$

By combining Equations D2 and D3, the Equation D2 can be converted to:

$$A = 2\pi R^2(\cos\theta_2 - \cos\theta_1) \quad (D4)$$

Equation D4 shows the area of the co-latitude interval in 3-D, A , has a positive correlation with $\cos\theta_2 - \cos\theta_1$, that is, $A \propto (\cos\theta_2 - \cos\theta_1)$. Moreover, the number frequency density, Φ , is a function of A (Equation D1). Therefore, in this study, we calculate the number frequency density, Φ , at a given co-latitude interval using:

$$\Phi = \frac{f}{\cos\theta_2 - \cos\theta_1} \quad (D5)$$

Appendix E: Deformation Mechanism Maps

Goldsby (2006) and Durham et al. (2010) used a deformation mechanism map to illustrate the relevance of dislocation creep and GBS-limited creep in experimentally and naturally deformed ice. Deformation mechanism maps were introduced to summarize information about the range of dominance of distinct deformation mechanisms in a polycrystalline solid (Ashby, 1972; Frost & Ashby, 1982). Deformation mechanism maps display the relationship between the three macroscopic variables: stress (y -axis), grain size (x -axis) and strain rate (contours with dashed lines) at different temperatures (Figure 7). The dislocation creep regime and GBS-limited creep regime are separated by a boundary displayed as a heavy black solid line, along which both mechanisms have an equal contribution to the total strain rate (Figure 7). At each temperature, strain rate contours were calculated using corresponding flow law parameters (Table 3) for dislocation creep (Equation 4) and GBS-limited creep regime (Equation 7). The reader is reminded that the deformation mechanism boundary (displayed as a heavy black solid line) is not a separation of deformation mechanisms, the deformation mechanism regime indicates the dominant deformation mechanism. Dashed colored lines represent the dislocation creep strain rate as ratio to the GBS-limited creep strain rate or the GBS-creep strain rate as ratio to the dislocation creep strain rate. For example, the dark-pink dashed line suggests dislocation creep strain rate is 100

times of the GBS strain rate; the red dashed line suggests GBS strain rate is 100 times of the dislocation creep strain rate (Figure 7).

We superposed stress-grain size points from experimental data from this study and published literatures (Fan et al., 2020; Jacka & Li, 1994; Jacka & Maccagnan, 1984; Vaughan et al., 2017; Table 7, Figure 7). The stress from this study, Vaughan et al. (2017) and Fan et al. (2020) is differential axial stress. The stress from Jacka and Maccagnan (1984) and Jacka and Li (1994), were converted from reported octahedral shear stress, τ_{oct} , using:

$$\sigma = \frac{3}{\sqrt{2}} \tau_{oct} \quad (E1)$$

For data from this study, Vaughan et al. (2017) and Fan et al. (2020), D_{avg} is the median grain size. For data from Jacka and Maccagnan (1984), the averaged grain size, D_{avg} , is taken directly from the paper. The D_{avg} from Jacka and Maccagnan (1984) is calculated using mean linear intercept method and $D_{avg} = 1.75L/N$, where L is the length of linear transverse, N is the number of grains intercepted by the linear transverse. For data from Jacka and Li (1994), the average grain size, D_{avg} , is calculated from averaged grain area A , using:

$$D_{ave} = 2 \times \sqrt{\frac{A}{\pi}} \quad (E2)$$

Points projected using stress-grain size relationships correspond to estimated strain rates as constrained by the strain rate contours (thin solid black lines) in deformation mechanism maps (Figure 7). Jacka and Li (1994) only reports a general strain range of their samples (>0.15).

Conflict of Interest

The authors declare no conflicts of interest relevant to this study.

Data Availability Statement

Data can be obtained via <https://doi.org/10.6084/m9.figshare.13456550> (Fan et al., 2020).

Acknowledgments

We are thankful to Pat Langhorne for providing the cold-room facility at University of Otago. This work was supported by a NASA fund (grant no. NNX15AM69G) to David L. Goldsby and two Marsden Funds of the Royal Society of New Zealand (grant nos. UOO1116, UOO052) to David J. Prior. Sheng Fan was supported by the University of Otago doctoral scholarship, the Antarctica New Zealand doctoral scholarship, a research grant from New Zealand Ministry of Business, Innovation and Employment through the Antarctic Science Platform (ANTA1801) (grant no. ASP-023-03), and a New Zealand Antarctic Research Institute (NZARI) Early Career Researcher Seed Grant (grant no. NZARI 2020-1-5). We thank Christopher J. L. Wilson and an anonymous reviewer and editor Yves Bernabe for their insightful reviews and editorial handling that helped to improve the manuscript.

References

- Alley, R. B. (1992). Flow-law hypotheses for ice-sheet modeling. *Journal of Glaciology*, 38(129), 245–256. <https://doi.org/10.3189/S0022143000003658>
- Ashby, M. F. (1972). A first report on deformation-mechanism maps. *Acta Metallurgica*, 20(7), 887–897. [https://doi.org/10.1016/0001-6160\(72\)90082-X](https://doi.org/10.1016/0001-6160(72)90082-X)
- Azuma, N. (1994). A flow law for anisotropic ice and its application to ice sheets. *Earth and Planetary Science Letters*, 128(3–4), 601–614. [https://doi.org/10.1016/0012-821X\(94\)90173-2](https://doi.org/10.1016/0012-821X(94)90173-2)
- Azuma, N. (1995). A flow law for anisotropic polycrystalline ice under uniaxial compressive deformation. *Cold Regions Science and Technology*, 23(2), 137–147. [https://doi.org/10.1016/0165-232X\(94\)00011-L](https://doi.org/10.1016/0165-232X(94)00011-L)
- Azuma, N., Miyakoshi, T., Yokoyama, S., & Takata, M. (2012). Impeding effect of air bubbles on normal grain growth of ice. *Journal of Structural Geology*, 42(C), 184–193. <https://doi.org/10.1016/j.jsg.2012.05.005>
- Azuma, N., Wang, Y., Mori, K., Narita, H., Hondoh, T., Shoji, H., & Watanabe, O. (1999). Textures and fabrics in the Dome F (Antarctica) ice core. *Annals of Glaciology*, 29, 163–168. <https://doi.org/10.3189/172756499781821148>
- Bachmann, F., Hielscher, R., & Schaeben, H. (2011). Grain detection from 2d and 3d EBSD data—Specification of the MTEX algorithm. *Ultra-microscopy*, 111(12), 1720–1733. <https://doi.org/10.1016/j.ultramic.2011.08.002>
- Bachtiar, E. V., Sanabria, S. J., Mittag, J. P., & Niemz, P. (2017). Moisture-dependent elastic characteristics of walnut and cherry wood by means of mechanical and ultrasonic test incorporating three different ultrasound data evaluation techniques. *Wood Science and Technology*, 51(1), 47–67. <https://doi.org/10.1007/s00226-016-0851-z>
- Behn, M., Goldsby, D., & Hirth, G. (2020). The role of grain-size evolution on the rheology of ice: Implications for reconciling laboratory creep data and the Glen flow law. *The Cryosphere Discussions*, (November), 1–31. <https://doi.org/10.5194/tc-2020-295>
- Bestmann, M., & Prior, D. J. (2003). Intragranular dynamic recrystallization in naturally deformed calcite marble: Diffusion accommodated grain boundary sliding as a result of subgrain rotation recrystallization. *Journal of Structural Geology*, 25(10), 1597–1613. [https://doi.org/10.1016/S0191-8141\(03\)00006-3](https://doi.org/10.1016/S0191-8141(03)00006-3)
- Bons, P. D., & Cox, S. J. D. (1994). Analogue experiments and numerical modelling on the relation between microgeometry and flow properties of polyphase materials. *Materials Science and Engineering A*, 175(1–2), 237–245. [https://doi.org/10.1016/0921-5093\(94\)91063-4](https://doi.org/10.1016/0921-5093(94)91063-4)
- Budd, W. F., & Jacka, T. H. (1989). A review of ice rheology for ice sheet modelling. *Cold Regions Science and Technology*, 16(2), 107–144. [https://doi.org/10.1016/0165-232X\(89\)90014-1](https://doi.org/10.1016/0165-232X(89)90014-1)

- Burlini, L., & Bruhn, D. (2005). *High-strain Zones: Laboratory Perspectives on Strain Softening during Ductile Deformation* (Vol. 245, pp. 1–24). Geological Society Special Publication. <https://doi.org/10.1144/GSL.SP.2005.245.01.01>
- Castelnau, O., Duval, P., Lebensohn, R. A., & Canova, G. R. (1996). Viscoplastic modeling of texture development in polycrystalline ice with a self-consistent approach: Comparison with bound estimates. *Journal of Geophysical Research B: Solid Earth*, 101(6), 13851–13868. <https://doi.org/10.1029/96jb00412>
- Cole, D. M. (1979). Preparation of polycrystalline ice specimens for laboratory experiments. *Cold Regions Science and Technology*, 1(2), 153–159. [https://doi.org/10.1016/0165-232X\(79\)90007-7](https://doi.org/10.1016/0165-232X(79)90007-7)
- Cross, A. J., Olree, E., Couvy, H., & Skemer, P. (2020). How does viscosity contrast influence phase mixing and strain localization? *Journal of Geophysical Research: Solid Earth*, 125(8), 1–20. <https://doi.org/10.1029/2020JB020323>
- Cross, A. J., & Skemer, P. (2017). Ultramylonite generation via phase mixing in high-strain experiments. *Journal of Geophysical Research: Solid Earth*, 122(3), 1744–1759. <https://doi.org/10.1002/2016JB013801>
- Cross, A. J., & Skemer, P. (2019). Rates of Dynamic Recrystallization in Geologic Materials. *Journal of Geophysical Research: Solid Earth*, 124(2), 1324–1342. <https://doi.org/10.1029/2018JB016201>
- Cuffey, K. M., & Paterson, W. S. B. (2010). *The Physics of glaciers* (4th ed.). Butterworth-Heinemann.
- De La Chapelle, S., Milsch, H., Castelnau, O., & Duval, P. (1999). Compressive creep of ice containing a liquid intergranular phase: Rate-controlling processes in the dislocation creep regime. *Geophysical Research Letters*, 26(2), 251–254. <https://doi.org/10.1029/1998GL900289>
- Derby, B., & Ashby, M. F. F. (1987). On dynamic recrystallisation. *Scripta Metallurgica*, 21(6), 879–884. [https://doi.org/10.1016/0036-9748\(87\)90341-3](https://doi.org/10.1016/0036-9748(87)90341-3)
- Drury, M. R. (2005). Dynamic recrystallization and strain softening of olivine aggregates in the laboratory and the lithosphere. *Geological Society - Special Publications*, 243(2), 143–158. <https://doi.org/10.1144/GSL.SP.2005.243.01.11>
- Durham, W. B., Heard, H. C., & Kirby, S. H. (1983). Experimental deformation of polycrystalline H₂O ice at high pressure and low temperature: Preliminary results. *Journal of Geophysical Research*, 88(S01), B377. <https://doi.org/10.1029/JB088iS01p0B377>
- Durham, W. B., Kirby, S. H., & Stern, L. A. (1992). Effects of dispersed particulates on the rheology of water ice at planetary conditions. *Journal of Geophysical Research*, 97(E12), 20883. <https://doi.org/10.1029/92je02326>
- Durham, W. B., Prieto-Ballesteros, O., Goldsby, D. L., & Kargel, J. S. (2010). Rheological and thermal properties of icy materials. *Space Science Reviews*, 153(1–4), 273–298. <https://doi.org/10.1007/s11214-009-9619-1>
- Duval, P. (1977). The role of the water content on the creep rate of polycrystalline ice, 118, 29–33.
- Duval, P. (1979). Creep and recrystallization of polycrystalline ice. *Bulletin de Mineralogie*, 102(2), 80–85. <https://doi.org/10.3406/bulmi.1979.7258>
- Duval, P., Ashby, M. F., & Anderman, I. (1983). Rate-controlling processes in the creep of polycrystalline ice. *Journal of Physical Chemistry*, 87(21), 4066–4074. <https://doi.org/10.1021/j100244a014>
- Eichler, J., Kleitz, I., Bayer-Giraldi, M., Jansen, D., Kipfstuhl, S., Shigeyama, W., et al. (2017). Location and distribution of micro-inclusions in the EDML and NEEM ice cores using optical microscopy and in situ Raman spectroscopy. *Cryosphere*, 11(3), 1075–1090. <https://doi.org/10.5194/tc-11-1075-2017>
- Fan, S., Hager, T. F., Prior, D. J., Cross, A. J., Goldsby, D. L., Qi, C., et al. (2020). Temperature and strain controls on ice deformation mechanisms: Insights from the microstructures of samples deformed to progressively higher strains at –10, –20 and –30°C. *The Cryosphere*, 14(11), 3875–3905. <https://doi.org/10.5194/tc-14-3875-2020>
- Fan, S., Prior, D. J., Cross, A. J., Goldsby, D. L., Hager, T. F., Negrini, M., & Qi, C. (2021). Using grain boundary irregularity to quantify dynamic recrystallization in ice. *Acta Materialia*, 209, 116810. <https://doi.org/10.1016/j.actamat.2021.116810>
- Fan, S., Prior, D. J., Hager, T. F., Cross, A. J., Goldsby, D. L., & Negrini, M. (2021). Kinking facilitates grain nucleation and modifies crystallographic preferred orientations during high-stress ice deformation. *Earth and Planetary Science Letters*, 572, 117136. <https://doi.org/10.1016/j.epsl.2021.117136>
- Freeman, B., & Ferguson, C. C. (1986). Deformation mechanism maps and micromechanics of rocks with distributed grain sizes. *Journal of Geophysical Research*, 91(B3), 3849–3860. <https://doi.org/10.1029/jb091ib03p03849>
- Frost, H. J., & Ashby, M. F. (1982). *Deformation mechanism maps: The plasticity and creep of metals and ceramics*. Pergamon Press. Retrieved from <https://engineering.dartmouth.edu/defmech/>
- Fujita, S., Hirabayashi, M., Goto-Azuma, K., Dallmayr, R., Satow, K., Zheng, J., & Dahl-Jensen, D. (2014). Densification of layered firn of the ice sheet at NEEM, Greenland. *Journal of Glaciology*, 60(223), 905–921. <https://doi.org/10.3189/2014JoG14J006>
- Gammon, P. H., Kieft, H., Clouter, M. J., & Denner, W. W. (1983). Elastic constants of artificial and natural ice samples by Brillouin spectroscopy. *Journal of Glaciology*, 29(103), 433–460. <https://doi.org/10.1017/S0022143000030355>
- Gao, X. Q., & Jacka, T. H. (1987). Approach To Similar Tertiary Creep Rates for Antarctic Core Ice and Laboratory Prepared Ice. *Journal de Physique. Colloques*, 48(3), 289. <https://doi.org/10.1051/jphyscol:1987141>
- Gerbi, C., Mills, S., Clavette, R., Campbell, S., Bernsen, S., Clemens-Sewall, D., et al. (2021). Microstructures in a shear margin: Jarvis Glacier, Alaska. *Journal of Glaciology*, 1, 1163–1176. <https://doi.org/10.1017/jog.2021.62>
- Ghosh, A. K., & Raj, R. (1981). Grain size distribution effects in superplasticity. *Acta Metallurgica*, 29(4), 607–616. [https://doi.org/10.1016/0001-6160\(81\)90142-5](https://doi.org/10.1016/0001-6160(81)90142-5)
- Glen, J. W. (1955). The creep of polycrystalline ice. *Proceedings of the Royal Society of London - Series A: Mathematical and Physical Sciences*, 228(1175), 519–538. <https://doi.org/10.1098/rspa.1955.0066>
- Goldsby, D. L. (2006). Superplastic Flow of Ice Relevant to Glacier and Ice-Sheet Mechanics. In *Glacier science and environmental change* (pp. 308–314). Blackwell Publishing. <https://doi.org/10.1002/9780470750636.ch60>
- Goldsby, D. L., & Kohlstedt, D. L. (1997). Grain boundary sliding in fine-grained Ice I. *Scripta Materialia*, 37(9), 1399–1406. [https://doi.org/10.1016/S1359-6462\(97\)00246-7](https://doi.org/10.1016/S1359-6462(97)00246-7)
- Goldsby, D. L., & Kohlstedt, D. L. (2001). Superplastic deformation of ice: Experimental observations. *Journal of Geophysical Research*, 106(B6), 11017–11030. <https://doi.org/10.1029/2000jb900336>
- Gordon, R. B. (1971). Observation of crystal plasticity under high pressure with applications to the Earth's mantle. *Journal of Geophysical Research*, 76(5), 1248–1254. <https://doi.org/10.1029/JB076i005p01248>
- Gow, A. J., & Williamson, T. (1976). Rheological implications of the internal structure and crystal fabrics of the West Antarctic ice sheet as revealed by deep core drilling at Byrd Station. *Geological Society of America Bulletin*, 87(12), 1665. [https://doi.org/10.1130/0016-7606\(1976\)87<1665:riotis>2.0.co;2](https://doi.org/10.1130/0016-7606(1976)87<1665:riotis>2.0.co;2)
- Griggs, D. T., & Blacic, J. D. (1965). Quartz: Anomalous Weakness of Synthetic Crystals. *Science*, 147(3655), 292–295. <https://doi.org/10.1126/science.147.3655.292>

- Hammonds, K., & Baker, I. (2018). The Effects of H₂SO₄ on the Mechanical Behavior and Microstructural Evolution of Polycrystalline Ice. *Journal of Geophysical Research: Earth Surface*, 123(3), 535–556. <https://doi.org/10.1002/2017JF004335>
- Hansen, L. N., Zimmerman, M. E., & Kohlstedt, D. L. (2012). The influence of microstructure on deformation of olivine in the grain-boundary sliding regime. *Journal of Geophysical Research*, 117(B9), 117–149. <https://doi.org/10.1029/2012jb009305>
- Haseloff, M., Hewitt, I. J., & Katz, R. F. (2019). Englacial Pore Water Localizes Shear in Temperate Ice Stream Margins. *Journal of Geophysical Research: Earth Surface*, 124(11), 2521–2541. <https://doi.org/10.1029/2019JF005399>
- Heard, H. C., Durham, W. B., Boro, C. O., & Kirby, S. H. (1990). A triaxial deformation apparatus for service at 77 ≤ T ≤ 273 K. In: *The Brittle-Ductile Transition in Rocks* (Vol. 56, pp. 225–228). <https://doi.org/10.1029/GM056p0225>
- Herwegh, M., Linckens, J., Ebert, A., Berger, A., & Brodhag, S. H. (2011). The role of second phases for controlling microstructural evolution in polymineralic rocks: A review. *Journal of Structural Geology*, 33(12), 1728–1750. <https://doi.org/10.1016/j.jsg.2011.08.011>
- Hill, R., Lee, E. H., & Tupper, S. J. (1947). The theory of combined plastic and elastic deformation with particular reference to a thick tube under internal pressure. *Proceedings of the Royal Society of London - Series A: Mathematical and Physical Sciences*, 191(1026), 278–303. <https://doi.org/10.1098/rspa.1947.0116>
- Hirth, G., & Kohlstedt, D. L. (1995). Experimental constraints on the dynamics of the partially molten upper mantle 2. Deformation in the dislocation creep regime. *Journal of Geophysical Research*, 100(B8), 1981–2001. <https://doi.org/10.1029/95jb01292>
- Holtzman, B. K., Chrysochoos, A., & Daridon, L. (2018). A thermomechanical framework for analysis of microstructural evolution: Application to olivine rocks at high temperature. *Journal of Geophysical Research: Solid Earth*, 123(10), 8474–8507. <https://doi.org/10.1029/2018JB015613>
- Hruby, K., Gerbi, C., Koons, P., Campbell, S., Martín, C., & Hawley, R. (2020). The impact of temperature and crystal orientation fabric on the dynamics of mountain glaciers and ice streams. *Journal of Glaciology*, 66(259), 755–765. <https://doi.org/10.1017/jog.2020.44>
- Humphreys, F. J., Hatherly, M., & Rollett, A. (2017). *Recrystallization and related annealing phenomena*. Elsevier Ltd. Retrieved from Third. <https://www.sciencedirect.com/book/9780080982359/recrystallization-and-related-annealing-phenomena>.
- Hunter, P., Meyer, C., Minchew, B., Haseloff, M., & Rempel, A. (2021). Thermal controls on ice stream shear margins. *Journal of Glaciology*, 67(263), 435–449. <https://doi.org/10.1017/jog.2020.118>
- Jacka, T. H., & Li, J. (1994). The steady-state crystal size of deforming ice. *Annals of Glaciology*, 20, 13–18. <https://doi.org/10.3189/1994aog20-1-13-18>
- Jacka, T. H., & Li, J. (2000). Flow rates and crystal orientation fabrics in compression of polycrystalline ice at low temperatures and stresses. In *International symposium on Physics of ice core records* (pp. 83–102). Hokkaido University Press. Retrieved from <http://hdl.handle.net/2115/32463>
- Jacka, T. H., & Maccagnan, M. (1984). Ice crystallographic and strain rate changes with strain in compression and extension. *Cold Regions Science and Technology*, 8(3), 269–286. [https://doi.org/10.1016/0165-232X\(84\)90058-2](https://doi.org/10.1016/0165-232X(84)90058-2)
- Jansen, D., Llorens, M. G., Westhoff, J., Steinbach, F., Kipfstuhl, S., Bons, P. D., et al. (2016). Small-scale disturbances in the stratigraphy of the NEEM ice core: Observations and numerical model simulations. *Cryosphere*, 10(1), 359–370. <https://doi.org/10.5194/tc-10-359-2016>
- Jones, S. J. (1967). Softening of ice crystals by dissolved fluoride ions. *Physics Letters A*, 25(5), 366–367. [https://doi.org/10.1016/0375-9601\(67\)90702-5](https://doi.org/10.1016/0375-9601(67)90702-5)
- Jones, S. J., & Glen, J. W. (1969). The effect of dissolved impurities on the mechanical properties of ice crystals. *Philosophical Magazine*, 19(157), 13–24. <https://doi.org/10.1080/14786436908217758>
- Journaux, B., Kalousová, K., Sofin, C., Tobie, G., Vance, S., Saur, J., et al. (2020). Large Ocean Worlds with High-Pressure Ices. *Space Science Reviews*, 216(1). <https://doi.org/10.1007/s11214-019-0633-7>
- Kamb, B. (2001). Basal Zone of the West Antarctic Ice Streams and its Role in Lubrication of Their Rapid Motion. In R. B. Alley, & R. A. Bindshadler (Eds.), *Antarctic research series* (Vol. 77, pp. 157–199). American Geophysical Union. <https://doi.org/10.1029/AR077p0157>
- Karato, S.-I., Paterson, M. S., & FitzGerald, J. D. (1986). Rheology of synthetic olivine aggregates: Influence of grain size and water. *Journal of Geophysical Research*, 91(B8), 8151. <https://doi.org/10.1029/JB091iB08p08151>
- Kronenberg, A. K., & Tullis, J. (1984). Flow strengths of quartz aggregates: Grain size and pressure effects due to hydrolytic weakening. *Journal of Geophysical Research*, 89(B6), 4281–4297. <https://doi.org/10.1029/jb089iB06p04281>
- Kuiper, E. J. N., De Bresser, J. H. P., Drury, M. R., Eichler, J., Pennock, G. M., & Weikusat, I. (2020). Using a composite flow law to model deformation in the NEEM deep ice core, Greenland-Part 2: The role of grain size and premelting on ice deformation at high homologous temperature. *Cryosphere*, 14(7), 2449–2467. <https://doi.org/10.5194/tc-14-2449-2020>
- Kuiper, E. J. N., Weikusat, I., De Bresser, J. H. P., Jansen, D., Pennock, G. M., & Drury, M. R. (2020). Using a composite flow law to model deformation in the NEEM deep ice core, Greenland-Part 1: The role of grain size and grain size distribution on deformation of the upper 2207m. *Cryosphere*, 14(7), 2429–2448. <https://doi.org/10.5194/tc-14-2429-2020>
- Li, J., Jacka, T. H., & Budd, W. F. (1996). Deformation rates in combined compression and shear for ice which is initially isotropic and after the development of strong anisotropy. *Annals of Glaciology*, 23, 247–252. <https://doi.org/10.1017/s0260305500013501>
- Lile, R. C. (1978). The effect of anisotropy on the creep of polycrystalline ice. *Journal of Glaciology*, 21(85), 475–483. <https://doi.org/10.3189/S0022143000033621>
- Little, T. A., Prior, D. J., Toy, V. G., & Lindroos, Z. R. (2015). The link between strength of lattice preferred orientation, second phase content and grain boundary migration: A case study from the Alpine Fault zone, New Zealand. *Journal of Structural Geology*, 81(C), 59–77. <https://doi.org/10.1016/j.jsg.2015.09.004>
- Llorens, M. G., Grier, A., Bons, P. D., Roessiger, J., Lebensohn, R., Evans, L., & Weikusat, I. (2016). Dynamic recrystallisation of ice aggregates during co-axial viscoplastic deformation: A numerical approach. *Journal of Glaciology*, 62(232), 359–377. <https://doi.org/10.1017/jog.2016.28>
- Lopez-Sanchez, M. A. (2020). Which average, how many grains, and how to estimate robust confidence intervals in unimodal grain size populations. *Journal of Structural Geology*, 135, 104042. <https://doi.org/10.1016/j.jsg.2020.104042>
- Lopez-Sanchez, M. A., & Llana-Fúnez, S. (2016). An extension of the Saltykov method to quantify 3D grain size distributions in mylonites. *Journal of Structural Geology*, 93, 149–161. <https://doi.org/10.1016/j.jsg.2016.10.008>
- Lutz, F., Eccles, J., Prior, D. J., Craw, L., Fan, S., Hulbe, C., et al. (2020). Constraining ice shelf anisotropy using shear wave splitting measurements from active-source borehole seismics. *Journal of Geophysical Research: Earth Surface*, 125(9), 1–18. <https://doi.org/10.1029/2020JF005707>
- McQueen, H. J., & Jonas, J. J. (1975). Recovery and recrystallization during high temperature deformation. In: *Plast deform of mater* (Vol. 6, pp. 393–493). ACADEMIC PRESS, INC. <https://doi.org/10.1016/B978-0-12-341806-7.50014-3>
- Mellor, M., & Cole, D. M. (1982). Deformation and failure of ice under constant stress or constant strain-rate. *Cold Regions Science and Technology*, 5(3), 201–219. [https://doi.org/10.1016/0165-232X\(82\)90015-5](https://doi.org/10.1016/0165-232X(82)90015-5)
- Morland, L. W., & Staroszczyk, R. (2009). Ice viscosity enhancement in simple shear and uni-axial compression due to crystal rotation. *International Journal of Engineering Science*, 47(11–12), 1297–1304. <https://doi.org/10.1016/j.jengsci.2008.09.011>

- Obbard, R. W., & Baker, I. (2007). The microstructure of meteoric ice from Vostok, Antarctica. *Journal of Glaciology*, 53(180), 41–62. <https://doi.org/10.3189/172756507781833901>
- Piazolo, S., Wilson, C. J. L., Luzin, V., Brouzet, C., & Peternell, M. (2013). Dynamics of ice mass deformation: Linking processes to rheology, texture, and microstructure. *Geochemistry, Geophysics, Geosystems*, 14(10), 4185–4194. <https://doi.org/10.1002/ggge.20246>
- Placidi, L., Greve, R., Seddik, H., & Faria, S. H. (2010). Continuum-mechanical, Anisotropic Flow model for polar ice masses, based on an anisotropic Flow Enhancement factor. *Continuum Mechanics and Thermodynamics*, 22(3), 221–237. <https://doi.org/10.1007/s00161-009-0126-0>
- Poirier, J. P. (1982). On transformation plasticity. *Journal of Geophysical Research*, 87(B8), 6791–6797. <https://doi.org/10.1029/JB087iB08p06791>
- Prior, D. J., Lilly, K., Seidemann, M., Vaughan, M., Becroft, L., Easingwood, R., et al. (2015). Making EBSD on water ice routine. *Journal of Microscopy*, 259(3), 237–256. <https://doi.org/10.1111/jmi.12258>
- Qi, C., Goldsby, D. L., & Prior, D. J. (2017). The down-stress transition from cluster to cone fabrics in experimentally deformed ice. *Earth and Planetary Science Letters*, 471, 136–147. <https://doi.org/10.1016/j.epsl.2017.05.008>
- Raj, R., & Ashby, M. F. (1971). On grain boundary sliding and diffusional creep. *Metallurgical Transactions*, 2(4), 1113–1127. <https://doi.org/10.1007/BF02664244>
- Raj, R., & Ghosh, A. K. (1981). Micromechanical modelling of creep using distributed parameters. *Acta Metallurgica*, 29(2), 283–292. [https://doi.org/10.1016/0001-6160\(81\)90155-3](https://doi.org/10.1016/0001-6160(81)90155-3)
- Ranalli, G. (1984). Grain size distribution and flow stress in tectonites. *Journal of Structural Geology*, 6(4), 443–447. [https://doi.org/10.1016/0191-8141\(84\)90046-4](https://doi.org/10.1016/0191-8141(84)90046-4)
- Rathmann, N. M., & Lilien, D. A. (2021). Inferred basal friction and mass flux affected by crystal-orientation fabrics. *Journal of Glaciology*, 1–17. <https://doi.org/10.1017/jog.2021.88>
- Rutter, E. H. (1995). Experimental study of the influence of stress, temperature, and strain on the dynamic recrystallization of Carrara marble. *Journal of Geophysical Research*, 100(B12), 651–663. <https://doi.org/10.1029/95jb02500>
- Rutter, E. H. (1999). On the relationship between the formation of shear zones and the form of the flow law for rocks undergoing dynamic recrystallization. *Tectonophysics*, 303(1–4), 147–158. [https://doi.org/10.1016/S0040-1951\(98\)00261-3](https://doi.org/10.1016/S0040-1951(98)00261-3)
- Rutter, E. H., & Brodie, K. H. (1988). The role of tectonic grain size reduction in the rheological stratification of the lithosphere. *Geologische Rundschau*, 77(1), 295–307. <https://doi.org/10.1007/BF01848691>
- Sahagian, D. L., & Proussevitch, A. A. (1998). 3D particle size distributions from 2D observations: Stereology for natural applications. *Journal of Volcanology and Geothermal Research*, 84(3–4), 173–196. [https://doi.org/10.1016/S0377-0273\(98\)00043-2](https://doi.org/10.1016/S0377-0273(98)00043-2)
- Saltikov, S. A. (1967). The Determination of the Size Distribution of Particles in an Opaque Material from a Measurement of the Size Distribution of Their Sections. In H. Elias (Ed.), *Stereology* (Vol. 53, pp. 163–173). Springer Berlin Heidelberg. https://doi.org/10.1007/978-3-642-88260-9_31
- Scheil, E. (1931). Die Berechnung der Anzahl und Größenverteilung kugelförmiger Kristalle in undurchsichtigen Körpern mit Hilfe der durch einen ebenen Schnitt erhaltenen Schnittkreise. *Zeitschrift für Anorganische und Allgemeine Chemie*, 201(1), 259–264. <https://doi.org/10.1002/zaac.19312010123>
- Schmid, S. M., Panozzo, R., & Bauer, S. (1987). Simple shear experiments on calcite rocks: Rheology and microfabric. *Journal of Structural Geology*, 9(5–6), 747–778. [https://doi.org/10.1016/0191-8141\(87\)90157-X](https://doi.org/10.1016/0191-8141(87)90157-X)
- Schwartz, H. A. (1934). The metallographic determination of the size distribution of temper carbon nodules. *Metals Alloys*, 5, 139.
- Sellars, C. M. (1978). Recrystallization of metals during hot deformation. *Philosophical Transactions of the Royal Society of London - Series A: Mathematical and Physical Sciences*, 288(1350), 147–158. <https://doi.org/10.1098/rsta.1978.0010>
- Shoji, H., & Langway, C. C. (1984). Flow behavior of basal ice as related to modeling considerations. *Annals of Glaciology*, 5(c), 141–148. <https://doi.org/10.3189/1984AoG5-1-141-148>
- Shoji, H., & Langway, C. C. (1988). Flow-law parameters of the dye 3, Greenland, deep ice core. *Annals of Glaciology*, 10, 146–150. <https://doi.org/10.3189/s026030550000433x>
- Skemer, P., Warren, J. M., Kelemen, P. B., & Hirth, G. (2009). Microstructural and rheological evolution of a mantle shear zone. *Journal of Petrology*, 51(1–2), 43–53. <https://doi.org/10.1093/petrology/egp057>
- Smith, E. C., Baird, A. F., Kendall, J. M., Martín, C., White, R. S., Brisbourne, A. M., & Smith, A. M. (2017). Ice fabric in an Antarctic ice stream interpreted from seismic anisotropy. *Geophysical Research Letters*, 44(8), 3710–3718. <https://doi.org/10.1002/2016GL072093>
- Soleymani, H., Kidder, S., Hirth, G., & Garapić, G. (2020). The effect of cooling during deformation on recrystallized grain-size piezometry. *Geology*, 48(6), 531–535. <https://doi.org/10.1130/G46972.1>
- Steinbach, F., Bons, P. D., Griera, A., Jansen, D., Llorens, M. G., Roessiger, J., & Weikusat, I. (2016). Strain localization and dynamic recrystallization in the ice-air aggregate: A numerical study. *Cryosphere*, 10(6), 3071–3089. <https://doi.org/10.5194/tc-10-3071-2016>
- Ter Heege, J. H., De Bresser, J. H. P., & Spiers, C. J. (2004). Composite flow laws for crystalline materials with log-normally distributed grain size: Theory and application to olivine. *Journal of Structural Geology*, 26(9), 1693–1705. <https://doi.org/10.1016/j.jsg.2004.01.008>
- Treverrow, A., Budd, W. F., Jacka, T. H., & Warner, R. C. (2012). The tertiary creep of polycrystalline ice: Experimental evidence for stress-dependent levels of strain-rate enhancement. *Journal of Glaciology*, 58(208), 301–314. <https://doi.org/10.3189/2012JoG11J149>
- Tullis, T. E., Horowitz, F. G., & Tullis, J. (1991). Flow laws of polyphase aggregates from end-member flow laws. *Journal of Geophysical Research*, 96(B5), 8081–8096. <https://doi.org/10.1029/90JB02491>
- Urai, J. L., Means, W. D., & Lister, G. S. (1986). Dynamic recrystallization of minerals. In: *Mineral and Rock Deformation* (Vol. 36, pp. 161–199). Laboratory Studies. <https://doi.org/10.1029/GM036p0161>
- van der Veen, C. J., & Whillans, I. M. (1994). Development of fabric in ice. *Cold Regions Science and Technology*, 22(2), 171–195. [https://doi.org/10.1016/0165-232X\(94\)90027-2](https://doi.org/10.1016/0165-232X(94)90027-2)
- Vaughan, M. J., Prior, D. J., Jefferd, M., Brantut, N., Mitchell, T. M., & Seidemann, M. (2017). Insights into anisotropy development and weakening of ice from in situ P wave velocity monitoring during laboratory creep. *Journal of Geophysical Research: Solid Earth*, 122(9), 7076–7089. <https://doi.org/10.1002/2017JB013964>
- Warren, J. M., & Hirth, G. (2006). Grain size sensitive deformation mechanisms in naturally deformed peridotites. *Earth and Planetary Science Letters*, 248(1–2), 438–450. <https://doi.org/10.1016/j.epsl.2006.06.006>
- Weertman, J. (1983). Creep Deformation of Ice. *Annual Review of Earth and Planetary Sciences*, 11(1), 215–240. <https://doi.org/10.1146/annurev.ea.11.050183.001243>
- Weikusat, I., Jansen, D., Binder, T., Eichler, J., Faria, S. H., Wilhelms, F., et al. (20172086). Physical analysis of an Antarctic ice core-towards an integration of micro-and macrodynamics of polar ice. *Philosophical Transactions of the Royal Society A: Mathematical, Physical & Engineering Sciences*, 375, 20150347. <https://doi.org/10.1098/rsta.2015.0347>
- White, S. H., Burrows, S. E., Carreras, J., Shaw, N. D., & Humphreys, F. J. (1980). On mylonites in ductile shear zones. *Journal of Structural Geology*, 2(1–2), 175–187. [https://doi.org/10.1016/0191-8141\(80\)90048-6](https://doi.org/10.1016/0191-8141(80)90048-6)

- Wilson, C. J. L., Hunter, N. J. R., Luzin, V., Peternell, M., & Piaolo, S. (2019). The influence of strain rate and presence of dispersed second phases on the deformation behaviour of polycrystalline D2O ice. *Journal of Glaciology*, *65*(249), 101–122. <https://doi.org/10.1017/jog.2018.100>
- Wilson, C. J. L., & Peternell, M. (2012). Ice deformed in compression and simple shear: Control of temperature and initial fabric. *Journal of Glaciology*, *58*(207), 11–22. <https://doi.org/10.3189/2012JoG11J065>
- Wilson, C. J. L., Peternell, M., Piaolo, S., & Luzin, V. (2014). Microstructure and fabric development in ice: Lessons learned from in situ experiments and implications for understanding rock evolution. *Journal of Structural Geology*, *61*, 50–77. <https://doi.org/10.1016/j.jsg.2013.05.006>